CHAPTER 3

REPORT OF THE 1988

2-D INTERCOMPARISON WORKSHOP

Section 3.1 Introduction

This report documents the findings of the participants of the September 11-16, 1988 2-D Intercomparison Workshop held in Virginia Beach, VA. The descriptions of the results of the various models for the several model experiments were done at this meeting. Several groups of investigators have updated their contributions to the model database since the meeting, therefore, the conclusions of this report should be taken as preliminary.

Table 3-1 shows the various modeling groups and their respective acronym or legend which is used to refer to modeling results of that group in the rest of this conference proceedings.

Table 3-1. Modeling groups involved and legends for figures.

Legend	Modeling Group
AER -	Atmospheric and Environmental Research, Inc., Cambridge, MA (M.K.W. Ko, N.D. Sze, and D.K. Weisenstein) 2-D Chemistry Transport Model
AERI-	Atmospheric and Environmental Research, Inc., Cambridge, MA (M.K.W. Ko, H.R. Schneider, N.D. Sze, W.C. Wang, and D.K. Weisenstein) 2-D Interactive Model
CALJPL -	California Institute of Technology and Jet Propulsion Laboratory, Pasadena, CA (Y.L.Yung, D. Crisp, R.W. Zurek) 2-D Model
CAMBRAL-	Cambridge University and Rutherford Appleton Laboratory, Great Britain (J.A. Pyle, L.J. Gray, and R.S. Eckman) 2-D Model
CAO -	Central Aerological Observatory, U.S.S.R. (V. Philushakin, E. Zhadin) 2-D Model
CLKSON -	Clarkson University, Postdam, N.Y. (K.K. Tung, H. Yang, and E. Olaguer) 2-D Model
DUPONT -	E. I. Du Pont De Nemour & Company, Inc., Wilmington, DE (D. Fisher) 2-D Model
GISS -	Goddard Institute for Space Studies, New York, N.Y. (M.J. Prather, M.M. Garcia, and D. Rind) 1-D and 3-D Model
GSFC1 -	Goddard Space Flight Center, MD (P.D. Guthrie, C.H. Jackman, and T.L. Kucsera) 2-D Model
GSFC2 -	Goddard Space Flight Center, MD (C.H. Jackman, A.R. Douglass, R.S. Stolarski, and P.D. Guthrie) 2-D Model
LARC-	Langley Research Center, Hampton, VA (W.L. Grose, R.S. Eckman, R.E. Turner, and W.T. Blackshear) 3-D Model
LLNL -	Lawrence Livermore National Laboratory, Livermore, CA (D.J. Wuebbles, P.S. Connell, K.E. Grant, and R. Tarp) 2-D Model

Table 3-1 (continued)

MPIC -   Max Planck Institute for Chemistry, Mainz, Federal Republic of Germany (P. Crutzen and C. Bruehl) 2-D Model

MRI -   Meteorological Research Institute, Japan (T. Sasaki and Y. Makino) 2-D Model

NOCAR -   National Oceanic and Atmospheric Administration and the National Center for Atmospheric Research, Boulder, CO (S. Solomon, and R. Garcia) 2-D Model

OSLO -   University of Oslo, Oslo, Norway (I. Isaksen and F. Stordal) 2-D Model

WISCAR -   University of Wisconsin, Eau Claire, WI and National Center for Atmospheric Research, Boulder, CO (G. Brasseur, M. H. Hitchman, and A. DeRudder) 2-D Model

Section 3.2 Photochemistry and Radiation

Charles Jackman

Since radiation drives the chemistry and dynamics of the atmosphere, it is important to understand the differences that arise in the various workshop models among the radiation fundamental quantities. The photodissociation coefficients are used in the computation of the dissociation of important molecules of the atmosphere. This dissociation leads to production of odd oxygen (mainly ozone in the stratosphere) and to radical production, which in turn lead to a whole host of photochemistry; some of which results in ozone destruction. The radiative heating and cooling of the atmosphere results in wind patterns with upward winds associated with atmospheric heating and downward winds associated with atmospheric cooling. A good simulation of the radiation and its multitude of effects in the atmosphere is necessary in order to model atmospheric problems correctly.

Section 3.2.1 Photodissociation Coefficients

Guy Brasseur

An important quantity in the source terms of chemical compounds is the photodissociation frequency of atmospheric molecules J. The value

$$J(z,\chi) = \int_\lambda \sigma(\lambda) \; q(\lambda,z,\chi) \; d\lambda,$$

where σ is the cross section of the molecule under consideration and $q(\lambda,z,\chi)$ the solar irradiance at altitude z for a solar zenith angle χ. The determination of the irradiance field depends on the absorption of solar light by ozone and molecular oxygen, multiple scattering and albedo. Furthermore, most 2-D models use diurnal averages of the J-values, which have to be defined properly. The spectral integration is usually performed over defined spectral intervals (typically 500 cm^{-1} width) except in the region of the Schumann-Runge bands where parameterizations of the averaged atmospheric transmissions over given wavelength intervals are usually determined following different methods (Nicolet and Peetermans, 1980; Allen and Frederick, 1982).

The comparison of the coefficients provided by the different groups shows several substantial differences. In the case of the O_2 photodissociation coefficient, variations of the order of a factor 2 are found among the different models in the upper stratosphere. Factor of 5 differences are seen for J_{NO}. This is an indication that the penetration of solar radiation in the Schumann-Runge region is treated differently in the various models. Substantial differences are also found for the photodissociation coefficients of F-11 and F-12. A possible reason for these discrepancies is the temperature dependence of the CFC-cross sections which is not taken into account in all models. A comparison of results dealing with species which are sensitive to wavelengths subject to scattering (NO_2, HNO_3, $ClONO_2$) suggests substantial differences due to the approximate treatment of multiple scattering. These are noticeable in the lower stratosphere and in the troposphere but also at higher altitude. In the case of $ClONO_2$, for example, differences of a factor 2 are observed at 40 km altitude. The photodissociation coefficient of NO_2 does not vary substantially with altitude but is highly dependent on the value adopted for surface albedo and on the treatment of multiple scattering. Differences between the calculated J's are of the order of 50% or less. In the case of N_2O, the differences between calculated J's reach a factor of 2 at 30 km.

Finally, in the case of ozone, there is a 30-50 percent discrepancy among models at 40 km altitude but the differences are larger in the lower stratosphere, where multiple scattering plays an important role.

Clearly, the differences among models are too large and need to be reduced by a more detailed comparison of the input (cross-section, solar irradiance), the calculation techniques and the results. The modelers involved in the Virginia Beach meeting will run a few simple and specific cases and compare these results in the near future.

Section 3.2.2 <u>Comparison of UV Heating and IR Cooling in Two-Dimensional Models</u>

Susan Solomon

<u>UV Heating</u>

Stratospheric heating is provided almost entirely by absorption of incoming solar radiation by ozone. At low altitudes, this is dominated by the Chappuis bands in the visible part of the spectrum, while at high altitudes ($z>30$ km) absorption in the ultraviolet through the Hartley bands becomes important. Further, weak absorption by NO_2 and other trace species makes a small (order 2 to 10%) contribution to the total heating in the lower stratosphere.

Table 3-2 displays calculated heating rates at particular points from some of the models for fixed O_3 and temperature on 1 January. The models are all in excellent agreement at 50°S, 20 km, where the estimated heating rate is 0.6 K/day. This suggests that the treatment of the Chappuis bands is comparable in all the models. However, the heating rates near the stratopause differ by as much as 35%, suggesting that there are large differences in the treatment of UV radiation or diurnal averaging. The difference in high altitude heating rates are strongly latitude dependent, suggesting that diurnal averaging plays an important role.

<u>IR Cooling</u>

There are also substantial differences among models in terms of their calculated IR cooling. All of the models considered here include both CO_2 15µm and O_3 9.6µm cooling (see Table 3-3). Near the tropical tropopause, O_3 may contribute net heating through infrared emission (e.g. positive rather than negative tendency) depending on the vertical temperature structure in the troposphere and other parameters. Some models also include minor contributions from IR emission of CH_4, CF_2Cl_2, etc.

The minimum cooling rates calculated near the summer stratopause vary by more than 40%. It is somewhat surprising that such large variations are obtained here, since the cooling rate does not require diurnal averaging and since infrared cooling codes have already been extensively intercompared by climate studies and other assessments. Further work will be required to understand the origin of these differences.

It is also important to note that large differences in magnitude and even in sign are found for the net cooling near the tropical tropopause. The nature of the sign in this region is heavily dependent on 9.6µm O_3 cooling, suggesting substantial differences in the treatments used.

Only a few groups reported cooling rates for doubled CO_2 using the standardized atmosphere. From the point of view of assessment studies, the cooling in the extra-tropical lower stratosphere is of great importance, as it plays a major role in determining the total O_3 response to doubled CO_2. Although only a few models reported results for that particular study, those that did were in reasonable agreement.

Table 3-2. Heating Rates from Two-Dimensional Models (°K/d)

Model Parameter	CLKSON	NOCAR	MPIC	AERI	CAMBRAL	OSLO	LLNL	CALJPL	WISCAR
Maximum heating near summer stratosphere	20	20	20	21	15	17	14	16	12
Equatorial maximum heating	10	10	10	11	11	9	8.5	10	9.5
Equator, 30 km	2	2.5	2.4	3	3.5	2.5	2		3
50°S, 20 km	0.6	0.6	0.6	0.6	0.6		0.6		.0.65

47

Table 3-3. IR Cooling Rates from Two-Dimensional Models (°K/d)

Model Parameter	CLKSON	NOCAR	MPIC	AERI	CAMBRAL	OSLO	LNL	CAL/JPL	WISCAR	GISS
Maximum cooling near summer stratosphere	-13	-16	-14	-11	-12	-11	-12	-16	-13	-16
As above, doubled CO_2			-18	-15	-15		-15			-19
Tropical tropopause region, maximum value	+0.2	+0.1	+0.2	-0.4	+0.1	+0.23	+0.3	+0.2	+0.16	+0.1
Doubled CO_2, 50 mb, 60°S			-1.0	-1.2	-1.25		-1.2			
Doubled CO_2, 50 mb, 60°N			-0.6	-0.8	-0.6		-0.5			

48

Section 3.3   Transport

Paul Guthrie

The representation of transport of constituents by atmospheric motions plays a major role in determining the spatial and temporal distribution of ozone (and other species) in 2-D model simulations of the atmosphere. Transport affects ozone directly, by moving it among regions where its photochemical lifetime differs greatly, and indirectly, by determining the distributions of the precursors to the radicals which catalyze ozone destruction. As part of the Intercomparison we have sought to focus on the processes which drive the simulated air motions in our models, and on the direct effect of the resulting transport on specified artificial "tracer" distributions.

This section describes the results of four intercomparisons. The first is an examination of the net radiative heating produced by different models for specified distributions of ozone and temperature. This is directly relevant to the advective transport which dominates the models using a Residual Mean Circulation formulation; it is less relevant for models based on a Classical Eulerian formulation. Differences among models noted here arise from differences in methods of approximating the transfer of solar and terrestrial radiation through the atmosphere. The remaining three intercomparisons employ surrogates for different classes of atmospheric species. Tracer X has a tropospheric source and stratospheric sink, representing precursor species such as N_2O. Tracer Y is a conserved species and examines the evolution in time of the distribution of a purely inert substance subject only to model transport. Tracer Z has a stratospheric source and tropospheric sink representing an "ozone-like" species. By comparing the model simulations for these three tracer experiments we hope to gain insight into the sensitivity of simulated species distributions to the model treatments of transport without confusion due to different model treatments of chemistry. A comparison of tracer Z with the ozone simulation in each model is quite instructive in illustrating the effects of interactions of transport and chemistry on the ozone column density.

Section 3.3.1   Residual Circulation Inferred from Heating Rates

Rolando Garcia

Transport in two-dimensional models is due to advection by the mean meridional circulation and mixing, usually parameterized as eddy diffusion. By examining the net diabatic heating rates, it is possible to obtain an estimate of the upward component of the residual circulation $\bar{w}^*$ The thermodynamic equation in the residual mean formulation for isobaric coordinates.

$$\frac{\partial \bar{T}}{\partial t} + \bar{v}^* \frac{\partial \bar{T}}{\partial y} + \bar{w}^* \frac{HN^2}{R} = \bar{Q}_{net} \qquad (1)$$

can be approximated as a balance between net diabatic heating and adiabatic effect due to vertical motions, i.e.

$$\bar{w}^* \frac{HN^2}{R} = \bar{Q}_{net} \qquad (2)$$

49

This approximation is most easily justified near solstice (when $\partial \bar{T} / \partial t \approx 0$ and in the middle and lower stratosphere (where horizontal nonlinear advection $\bar{V}^* \bar{T}_y$ can be neglected). In isentropic coordinates the analog of eq. (2) is the full thermodynamic equation, so mean vertical motions can always be deduced from net heating rates, provided the latter is available on isentropic surfaces.

In what follows $\bar{Q}_{net}$ is used as a diagnostic of the vertical component of the residual circulation for the various 2-D models included in this intercomparison. Different 2-D models can be classified according to whether $\bar{Q}_{net}$ is specified externally or computed interactively. Implicit in externally specified $\bar{Q}_{net}$ distributions is the effect of wave processes which drive the atmosphere away from radiative equilibrium. If $\bar{Q}_{net}$ is computed interactively, its value depends ultimately on the specification or parameterization of wave driving.

Table 3-4 lists the various models included in this intercomparison, together with the method used to obtain $\bar{Q}_{net}$. Models with specified $\bar{Q}_{net}$ are somewhat more common at present than models wherein $\bar{Q}_{net}$ is computed interactively. The CLKSON model is a special case in that the net heating rate is obtained from computed UV heating and IR cooling based on a specified temperature distribution. Table 3-4 also notes whether any attempt is made to parameterize wave driving and eddy diffusion in a self-consistent fashion. For example, the CLKSON model wave driving is estimated from the zonal momentum equation,

$$\overline{v'q'} = -f\,\bar{v}^*$$

(3)

and $\overline{v'q'}$ is then parameterized as diffusion of mean potential vorticity,

$$K_{yy} = \frac{\overline{v'q'}}{q_y}$$

(4)

It should also be noted that in models wherein the circulation is specified at the lower boundary (e.g., NOCAR), an integrated EP flux divergence in the interior is implied. Briefly, from the steady-state balance

$$-f\,\bar{v} = \frac{1}{\rho}\nabla \cdot F$$

(5)

we can derive the relationship

$$\bar{\chi}^*(z_o) = \frac{1}{f\rho(z_o)}\int_{z_o}^{\infty} \nabla \cdot F \; dz$$

(6)

which says that the stream function at z_0 depends on the EP flux divergence throughout the interior of the model above z_0.

Regardless of whether $\bar{Q}_{net}$ is specified or computed, it is desirable that eddy diffusivities used in 2-D models should be consistent with the wave driving. It is not totally clear at present what is the best method for obtaining such consistency. The CLKSON model (which considers all wave driving to be due to non-linear effects, and hence to imply mixing), is an example of an approach to this self-consistency criterion. The validity of this approach in regions where thermal dissipation might be

50

not conserved) remains to be investigated.

The role of mixing cannot be assessed from an examination of $\bar{Q}_{net}$. The following comparison focuses on overall patterns of $\bar{Q}_{net}$ and on its magnitude in certain key regions as a means of comparing advective transport in various 2-D models. Figures on pages 205-211 show $\bar{Q}_{net}$ for January for all models listed in Table 3-4. Qualitatively, the overall patterns in most models are strongly similar, with upwelling in the summer upper stratosphere and downwelling throughout the winter stratosphere. In the lower stratosphere, there is upwelling in the tropics and downwelling in both summer and winter hemispheres.

More detailed examination of figures on pages 205-211 reveals significant differences among the various models. These are especially noticeable in the summer upper stratosphere, where most models show strong upwelling, but some of the models have much weaker upwelling, or even downwelling. Table 3-5 shows summer, high latitude vertical velocities near the summer stratopause (70°S, 1 mb) to further quantify this point. Upwelling in this region of the atmosphere is important because it determines the temperature of the summer stratopause and hence the ozone concentration there.

Table 3-5 also compares vertical velocities at the tropical tropopause (0°, 100 mb) and the high latitude, winter lower stratosphere (70°N, 50 mb). These locations are chosen for the presumed importance of vertical advection there (flux of source gases from the troposphere and advective control of the total ozone column at high latitudes). The vertical velocities implied by $\bar{Q}_{net}$ at these locations are generally in good agreement among models, especially in winter high latitudes.

The results presented here are only a rough indication of transport differences among models. It should be emphasized once again that eddy transport is not taken into account by this comparison, and that there are significant differences in the definition or parameterization of eddy diffusion in the various models. Nevertheless, vertical motions should have important effects in the distribution of constituents (and ozone in particular) and the present comparison indicates that differences in vertical advection among models could be significant, especially near the summer stratopause.

51

Table 3-4. Description of $\bar{Q}_{net}$ in each Model

<u>Model</u>	<u>Formulation</u>
AER	$\bar{Q}_{net}$ specified
AERI	$\bar{Q}_{net}$ computed. Wave driving from parameterized Raleigh friction and diffusion of potential vorticity.
CALJPL	$\bar{Q}_{net}$ specified from GFDL 3-D model. Eddy diffusion coefficients estimated from momentum balance.
CAMBRAL	$\bar{Q}_{net}$ computed; $\overline{u'v'}$ specified; $\overline{v'T'}$ parameterized in terms of K_{yy}, K_{yz} and mean temperature gradients.
CLKSON	$\bar{Q}_{net}$ computed, from specified temperature field. Eddy diffusion estimated from momentum balance.
GSFC1 (interactive)	$\bar{Q}_{net}$ computed.
GSFC2 (fast)	$\bar{Q}_{net}$ specified.
MRI	$\bar{Q}_{net}$ specified.
NOCAR	$\bar{Q}_{net}$ computed. $\bar{\chi}^*$ specified at lower boundary.
WISCAR	$\bar{Q}_{net}$ computed. Wave driving and diffusion obtained from planetary wave calculation.

Table 3-5. Vertical Velocities (cm/sec)

Model	0°, 100 mb	70°N, 50 mb	70°S, 1 mb	Comments
AER	0.3	-0.6	1.2	Strong summer-winter circulation
CALJPL	0.0	-0.5	0.5	Strong summer-winter circulation
CLKSON	0.5	-0.5	1.5	Strong summer-winter circulation
GSFC1	0.4	-0.5	0.2	Weak summer upwelling
GSFC2	0.2	-0.5	0.5	Strong summer-winter circulation
MRI	0.4	-0.4	1.0	Weak downwelling in winter upper stratosphere
NOCAR	0.2	-0.5	1.8	Strong summer-winter circulation
WISCAR	0.1	-0.4	-0.3	Weak summer upwelling (Downwelling above 3 mb at 70°S.)

Section 3.3.2 Tropospheric Source (X)

Yuk Yung

This experiment is designed to test three fundamental properties of the 2-D model:

(1) Advection
- (a) Equatorial upwelling
- (b) Pole-pole circulation

(2) Diffusion
- (a) K_{yy}
- (b) K_{zz}

(3) Lifetime of a chemical tracer.

From the morphology of the tracer distribution in various seasons we can deduce whether the advective and diffusive processes are strong or weak. {For a number of models the upper boundary is located near 60 km, therefore, the large discrepancies between the contour lines at the highest altitudes are not significant.} In Table 3-6 we provide a qualitative assessment of whether advection and diffusion in each model is strong or weak, and whether the pole-to-pole circulation is evident or not.

Table 3-7 summarizes the mixing ratio of X at the equator in June at 30 and 40 km. The values at 30 km in all models are dominated by the troposphere and are therefore very close to each other. The value at 40 km is an indication of the strength of the equatorial upwelling. Thus, AER has strong upwelling whereas WISCAR has less upwelling.

The mean lifetime of X is summarized in Table 3-8, along with the number cf years the models were run. It takes about 10 years for the steady-state distribution of X to be established. The mean lifetime is about 110 years, with about 30% spread among the various groups. There seems to be a qualitative correlation between models with fast circulation and shorter lifetimes. The lifetime of X is determined by (a) transport through the tropopause and by (b) transport to the middle stratosphere. To obtain a quantitative indication of the above processes, these three mass integrals should be investigated:

(i)   Total mass of X in model
(ii) Mass of X above 100 mb
(iii) Mass of X above 10 mb

Table 3-6. Qualitative Assessment of Advection and Diffusion in each Model

Model	Advection	Diffusion	Pole-Pole Circulation
AER	Strong	Weak	None
GSFC2	Average	Average	Strong
MRI	Weak	Strong	None
CALJPL	Strong	Average	Present
CLKSON	Average	Average	Present
WISCAR	Weak	Average	Weak (strong K_{zz} effects at high altitudes)
OSLO	Average	Average	Weak

Table 3-7. The Mixing Ratio of X at the Equator in June

Model	30 km	40 km
AER	7 (-10)*	2 (-10)
GSFC2	7 (-10)	3 (-11)
MRI	7 (-10)	3 (-11)
WISCAR	6 (-10)	4 (-11)
CALJPL	7.5 (-10)	3 (-10)
CLKSON	7 (-10)	1 (-10)
OSLO	6 (-10)	1 (-10)

* 7(-10) means 7×10^{-10}

Table 3-8. The Mean Lifetime of X

Model	Mean Lifetime (years)	# of Years Run
AER	103	15
GSFC2	127	15
CLKSON	97	10
WISCAR	109	3
CALJPL	122	9
OSLO	120	40
LLNL	109	10

Section 3.3.3 Time-dependent Source (Y)

Lesley Gray

Experiment Description

5x10¹⁰ kg of species Y (at. wt.=29 yields a global average of 1 ppmv) placed in the lower troposphere (>700 mb). No loss for species Y. Model experiment started January 1st and run for 5 years. This experiment highlights: (a) the speed with which each model achieves troposphere - stratosphere exchange, (b) the morphology of a passive tracer in the stratosphere, (c) the ability of each model to conserve mass.

Results

Figures on pages 222-246 show latitude-height distributions every 1/2 year (January 1st, July 1st), from each model. A general pattern of ascent in equatorial regions is evident. There is some variation in the speed of troposphere-stratosphere exchange among the models (which is quantified more fully below). For example, the distributions after six months show that the MRI, AER and LLNL models achieve a rapid transfer compared with the GSFC2 and CLKSON models. Once a sufficient amount of tracer has reached the stratosphere, a seasonal cycle in distribution is displayed by the models, with the maximum mixing ratios generally displaced off the equator into the summer hemisphere. There is some variation among the models in the strength of this seasonality. For example, the GSFC2 model exhibits strong evidence of a summer to winter circulation; the MRI model, on the other hand, shows a weak seasonal dependence, with a distribution that is almost symmetric about the equator in both January and July. The complicated pattern displayed by the GSFC2 model, for example in July of year 2, is probably a result of small values for K_{yy}, therefore, the bulge in the southern hemisphere in the region 25-35 km is a remnant of the southern hemisphere's peak six months previously. The well-defined equatorial peak in, e.g. the AER model, compared with the much broader distribution in the MRI model, can be attributed to (a) stronger equatorial upwelling, (b) weaker K_{yy} values or (c) a combination of both (a) and (b).

In Figure 3-1 the time-evolution of the 0.7 ppm contour at the equator is shown for each model. The time taken for the contour to traverse 10 km height intervals is tabulated in Table 3-9. From these time-estimates a value has been calculated for the annual-average- $\bar{w}$ that would be required to perform this transport. There is a large variation in the time taken to reach 20 km. This must be due to differences in the value of K_{zz} employed in the troposphere or in the strength of the equatorial upwelling in the troposphere. Note that the two models with slowest ascent to 20 km (GSFC2 and CLKSON) also have significantly smaller tropospheric K_{zz} values. Above 30 km, the AER, LLNL, and CLKSON models display rapid ascent while MRI has weak ascent. These observations are in good agreement with conclusions from the model intercomparison of net heating rates. For example, several of the models display a similar pattern of strong ascent below 20 km and above 30 km, with a region of weak ascent in the intervening region (20-30 km) coinciding with a region of reduced net heating rates between 20 and 30 km.

Table 3-9. Time taken for 0.7 ppm contour to traverse 10 km height intervals

	0-20 km	20-30 km	30-40 km	40-50 km	Average Tropospheric 20-50 km	K_{zz}
AER	0.7 yrs.	1.75 yrs.	0.8 yrs.	0.45 yrs.	0.31 mm s^{-1}	-10^5
GSFC2	2.0 yrs.	1.0 yrs. 0.29 mm s^{-1}	1.1 yrs. 0.29 mm s^{-1}	0.9 yrs. 0.35 mm s^{-1}	0.31 mm s^{-1}	-10^4
MRI	0.5 yrs.	1.5 yrs. 0.21 mm s^{-1}	3.0 yrs. 0.11 mm s^{-1}		0.14 mm s^{-1}	-10^5
LLNL	0.5 yrs.	1.8 yrs. 0.18 mm s^{-1}	0.9 yrs. 0.35 mm s^{-1}	0.5 yrs. 0.63 mm s^{-1}	0.34 mm s^{-1}	-10^5
CLKSON	1.5 yrs.	1.35 yrs. 0.23 mm s^{-1}	0.9 yrs. 0.35 mm s^{-1}	0.5 yrs. 0.63 mm s^{-1}	0.34 mm s^{-1}	0

57

Section 3.3.4 Stratospheric Source (Z)

K. K. Tung

The mixing ratio of Z for p<10 mb is specified at a large value (8 ppmv) in the stratosphere while its value is fixed near the lower boundary at a small value of 0.10 ppm for p>850 mb. The large value represents a stratospheric source, while the lower boundary acts as a tropospheric sink. At steady state (annually periodic), tracer Z in the region between p=850 mb and p=10 mb will equilibrate when the "production rate" (the amount of flux transported down from the source region) balances the "destruction rate" (the flux into the surface sink region).

In the absence of vertical transports, the column amount of Z should be approximately 60 Dobson units, uniform in latitude and in season, assuming that Z=0 in the middle layer: 850 mb > p > 10 mb. All models produce column amounts above 100 DU when the effect of transport is included even if one starts with the initial condition of Z=0 in the middle layer.

It is interesting to note that all models have 100 DU or more of Z over the equatorial region, where there is upwelling in most models. Apparently, the excess over 60 DU is caused either by vertical mixing down from the source region in models that have K_{zz}, and/or by high latitude downward advective transport from the source region followed by horizontal transports into the tropical region.

In the presence of transport below 10 mb, all models create an equatorial column minimum and high latitude maxima. Some models also produce seasonal behavior with high-latitude maximum in spring and minimum in fall, mirroring their respective simulations of column ozone presented in Section 3.4.2.

The AER model yields 120 DU in the equatorial region, while CALJPL, CLKSON, and GSFC2 produce values of Z about 40 DU higher in the same region. The present version of the AER model has a larger value of equatorial upwelling. The polar spring maximum for all 4 models are between 400 and 500 DU.

The LLNL model has 120 DU in the tropical region as in the AER model, but the high latitude maximum is a weaker 350 DU. Similar to the above mentioned models the seasonal behavior of spring maximum and fall minimum in high latitudes is clearly present in the LLNL model. However, LLNL appears to have larger amounts of Z in the southern hemisphere than in the northern hemisphere, in contrast to the behavior of its simulated column ozone.

The MRI model is distinctly different than all the other models in having a smaller global content (100 DU in the equatorial region and 300 DU over the poles) and a much weaker seasonal variation. The OSLO model has a low equatorial minimum of 100 DU, but the polar maxima are 400 DU. The seasonal behavior of spring maximum and fall minimum is present in the OSLO model in the Northern Hemisphere. In the Southern Hemisphere, however, the maximum occurs instead in winter. This behavior is consistent with its ozone simulation, and is probably caused by a discontinuity in its specified radiative heating rate near 25 km in the Southern Hemisphere winter.

The differences in the model results for Z are attributable to differences in model transport characteristics below 10 mb. The weak seasonal and latitudinal contrasts in the MRI model may be due to weak vertical circulation in that model near the 10 mb region. The AER model has a stronger vertical upwelling velocity in the equatorial region than most models. It tends to bring air depleted in Z by the surface sink to the region between 850 mb and 10 mb, resulting in a smaller value of Z in the equatorial region.

Although the Dobson map for Z resembles that for ozone simulated for each model, there is a significant difference between column Z and column ozone of some models. By design, the seasonal and latitudinal contrasts in tracer Z column can be attributed entirely to transports in the region below 10 mb. For ozone, however, seasonal variations in photochemical production and loss rates can also induce seasonal variation in the ozone column. In addition, transport above 10 mb affects the seasonal and latitudinal contrasts slightly. By comparing the Dobson maps for ozone and tracer Z, some ideas concerning the relative importance of these processes (vs. that of transport below 10 mb) can be discerned.

Section 3.4   Current Atmosphere: 1980

Malcolm Ko

Since all models have some adjustable parameters in their formulations, the real test of the performance of a model is not how it simulates the latitudinal and seasonal behavior of just one single trace gas, but how successful it is in simulating the behaviors of all the trace gases in a self-consistent manner. For models that are designed to predict the future response of O_3, validation of the present day O_3 distributions should be a prerequisite. With a large data base from satellite observations detailing the behavior of O_3, it is not surprising that most model results for O_3 appear quite similar. However, it is also necessary to ascertain that the present day behavior is obtained by correctly simulating the appropriate mechanisms. This is why there is a need to compare the simulated behavior of other trace gases.

The behavior of the column abundance of O_3 is sensitive to the transport treatment in the lower stratosphere. Apart from the experiments in Section 3.2 specifically designed to test the transport, examination of the behavior of the column abundances of HNO_3, HCl, and NO_2 will be useful as a consistency check particularly since observations are available for validation. The behavior of the source gases such as N_2O, CH_4, CCl_4, CH_3Cl, and CFC's are sensitive to the transport treatment in the middle and upper stratosphere. Comparison of the calculated lifetimes of those gases that are removed in the stratosphere also provides a measure of the strength of the circulation.

In this comparison, an attempt is made to isolate the effect of photochemical treatment by comparing separately the total odd nitrogen (NO_y) and the partitioning of the nitrogen species (i.e., NO/NO_2, NO_2/HNO_3 ratios). The same is also done for total chlorine (Cl_y) and the partitioning of the chlorine species. Although no comparison was made on the water vapor content, a comparison of the hydroxyl radicals provided information on the HO_x cycle.

Given the importance of the 40 km O_3 problem (that model calculated O_3 is smaller than observation), a special comparison was made on the species concentrations, photolysis rates, and reaction rates that would affect the concentration of O_3 at 40 km.

The simulated trace gas distribution from the models are presented in Chapter 6 of this report. These include:

> latitude and season plots of the column abundances of O_3, HNO_3, NO_2, and ClO
> latitude and altitude cross-sections of NO_y and Cl_y,
> latitude and altitude cross-sections of NO_x, NO, NO_2, HNO_3, N_2O_5, HNO_4, the ratio of NO/NO_2, HNO_3/NO_2, and NO_x/NO_y
> latitude and altitude cross-sections of ClO, HCl, $ClNO_3$, HOCl, the ratio of Cl/ClO, ClO/Cl_y and ClO/HCl
> latitude and altitude cross-sections of O_3, HO_2, H_2O_2, O, OH, the ratio of O/O_3 and OH/HO_2
> latitude and altitude cross-sections of N_2O, CH_4, F-11, F-12, CCl_4 and CH_3CCl_3.

There is no uniform criteria one can apply to all the model simulated results to quantify whether agreements among the models are good. Such a decision is based on subjective judgement and the sensitivity of the individual results on model parameters. The following discussion will concentrate more on the relevance of certain quantities selected for discussions rather than on detailed agreement and discrepancies among the models.

Section 3.4.1 The 40 km Ozone "Problem"

Charles Jackman

The odd oxygen (O_x) budget including all losses and production was compared at the 3 mbar level for three latitudes (-45°S, 0°, and 45°N) at two months (March and June). The 3 mbar level was chosen for three major reasons: 1) models have a problem in predicting the ozone amount at this altitude (models predict ozone values at a smaller level than measured), 2) production should approximately equal the loss for O_x at least at the equator, and 3) all four families (O_x, HO_x, NO_x, and Cl_x) are believed to be important for the loss of odd oxygen at this level. It was thought that by careful analysis of several models' output, additional insight into the ozone level problem would be possible.

Ten separate modelling groups took part in this intercomparison, some groups providing all the information at the three latitudes for both months, others providing information for a couple of latitudes, and still others providing limited information for a couple of latitudes. Since all ten modelling groups provided information at the equator for March, we focus on that point in this analysis.

We do, however, rely on other latitudes and June data to provide corroborative information as well. The ten groups included one 1-D model, eight 2-D models, and one 3-D model. The groups and acronyms used in the figures are given in Table 3-1.

The major items compared were the O_x production and loss terms. The production for O_x was defined to be $P(tot) = 2 J_1(O_2) [O_2]$. The loss terms $L(tot) = L(O_x) + L(HO_x) + L(NO_x) + L(Cl_x)$ were all taken from Johnston and Podolske [1978] and were defined to be $L(O_x) = 2 k_2 [O_3] [O]$, $L(HO_x) = 2 \{k_3 [HO_2] [O] + k_4 [HO_2] [O_3] + k_5 [H] [O_3] + k_6 [OH] [HO_2] + k_7 [HO_2] [HO_2] \}$, $L(NO_x) = 2 \{k_8 [NO_2] [O] + J_9 [NO_3]\}$, and $L(Cl_x) = 2 k_{10} [ClO] [O]$. Table 3-10 presents results of the comparison of the various models at the equator in March.

The ratio of the highest model value to the lowest model value was relatively small for $P(tot)$ and $L(tot)$, being 1.44 and 1.42, respectively. The variance among the various families was larger, varying from 1.47 for $L(O_x)$ to 2.64 for $L(Cl_x)$.

$P(tot)$ does approximately equal $L(tot)$ at the equator at 3 mbar in March for the various models which indicates a relative consistency in a given model and among the various models when comparing these O_x rates. The relative fraction of loss in a family is given in Figure 3-2 (a-d), where $L(O_x)/L(tot)$, $L(HO_x)/L(tot)$, $L(NO_x)/L(tot)$, and $L(Cl_x)/L(tot)$ are presented.

The $L(O_x)$ and $L(HO_x)$ are thought to be relatively consistent within the various models because of the good correlation that is apparent when $L(HO_x)$ is plotted as a function of $L(O_x)$ in Figure 3-3. Since H_2O, affecting only $L(HO_x)$, does not vary greatly among the models and O_3 and O influence both $L(O_x)$ and $L(HO_x)$, the good correspondence between $L(O_x)$ and $L(HO_x)$ was expected.

The $L(NO_x)$ is more complicated. Since $L(NO_x)$ depends on both NO_2 and O, and because both NO_2 and O have strong diurnal cycles with NO_2 being larger in the nighttime and O larger in the daytime, it is not clear what would happen in an intermodel comparison of $L(NO_x)$. We do find that NO_x ($NO+NO_2$) is not well correlated with its major production of $2 k_{11} [N_2O] [O(^1D)]$, but rather seems to asymptote for most models to values between 15 and 25 ppbv for larger NO_x production rates (see Figure 3-4). NO_x is very dependent on transport at 3 mbar and has an overall lifetime on the order of months (including both transport and chemistry). It is interesting that we find a variance in N_2O of over a factor of five and a range in NO_x of only about 50%.

The level of NO_x appears to be fairly robust, which is a surprising result considering the large variation in the circulation from model to model. A qualitative explanation is found by considering the ramifications of a weak and a strong circulation on NO_x behavior. A weak circulation will not move N_2O and NO_x upward or downward in the atmosphere very quickly, thus N_2O will be kept at a fairly small level at 3 mbar whereas NO_x will be allowed to increase to a moderately large (15-25 ppbv) equilibrium level. A strong circulation, on the other hand, will move N_2O and NO_x upward and downward in the atmosphere

very quickly, thus N_2O will reach a relatively large level at 3 mbar whereas NO_x will be constrained to an equilibrium level of 15-25 ppbv. The largest loss for NO_x or odd nitrogen in the atmosphere is transformation to HNO_3, transport to the troposphere, and subsequent rainout as constituent HNO_3. The equilibrium level for NO_x will be constrained by a balance between production through oxidation of N_2O and loss through the rainout of tropospheric HNO_3. One of the major keys to this equilibrium balance is the strength of the transport of NO_x away from its production region in the middle to upper stratosphere.

There is a fairly large disagreement in $L(Cl_x)$ among the models, most of the discrepancy arising from the large variation in the amount of Cl_x at 3 mbar. The fractional loss due to Cl_x then affects the relative fractions available to the other three families, O_x, HO_x, and NO_x.

Since $L(Cl_x)$, $L(NO_x)$, their relation to each other and to the losses from $L(O_x)$ and $L(HO_x)$ is complicated, we have taken a more detailed look at the results of five modeling groups which have fairly similar P(tot) values (variations only on the order of 5%), but which have a fairly large O_3 variation (on the order of 28%). The values of ten important rates and species are given in Table 3-11.

The most obvious correlation with ozone amount is an inverse correlation with $J(O_3 \, tot)$, etc. The model with the smallest $J(O_3 \, tot)$ [GSFC2] has the largest ozone and the model with the largest $J(O_3 \, tot)$ [MRI] has the smallest ozone. Other correlations involving absolute amounts of Cl_x and $L(Cl_x)$ are not so obvious, although there does seem to be some correspondence. The two models [AER and GSFC2] with the smallest amounts of Cl_x have the smallest $L(Cl_x)$ values and the two models [LLNL and MRI] with the largest amounts of Cl_x have the largest $L(Cl_x)$ values, however, this is only a very general relationship.

The reason for the relationship between $J(O_3 \, tot)$ and amount of O_3 is more easily envisioned when P(tot) is set equal to L(tot) and O_3 is solved for, including only the major terms. Using that approximation, we derive the following relationship

$$[O_3] = \frac{J_1[O_2] - k_3[HO_2][O] - k_8[NO_2][O] - k_{10}[ClO][O]}{k_2[O]} \qquad (7)$$

Now [O] is dependent on $J(O_3 \, tot)$ and $[O_3]$ through the equation

$$[O] = \frac{J(O_3 \, tot) \, [O_3]}{k_{12}[O_2] \, [M]} \qquad (8)$$

Using (8), we can rewrite (7) as

$$[O_3] = \frac{J_1[O_2] - f\{HO_x, NO_x, Cl_x, J(O_3 \, tot)\}}{g\{O_x, J(O_3 \, tot)\}} \qquad (9)$$

where

$$f\{HO_x, NO_x, Cl_x, J(O_3 \, tot)\} = \frac{J(O_3 \, tot)[O_3](k_3[HO_2] + k_8[NO_2] + k_{10}[ClO])}{k_{12}[O_2] \, [M]} \qquad (10)$$

and
$$g(O_x, J(O_3 \text{ tot})\} = k_2 J(O_3 \text{ tot}) [O_3] / k_{12}[O_2] [M] \qquad (11)$$

Ignoring the fact that (9) is a transcendental equation for the moment, we find that $[O_3]$ will be inversely related to $J(O_3$ tot) because of the influence of f and g which are directly proportional to $J(O_3$ tot). The numerator in (9) has f subtracted from $J_1[O_2]$ and then that result is divided by the denominator g. Generally, larger values of $J(O_3$ tot) mean smaller levels of $[O_3]$.

This relationship between $J(O_3$ tot) and $[O_3]$ can be understood in another way. P(tot) is independent of the O at a given level and more or less fixed with the sun angle, whereas most terms in L(tot) are directly proportional to the amount of O at that level. The greater the $J(O_3$ tot), the greater the O, but since P(tot) is approximately equal to L(tot) at the equator and O is directly proportional to O_3 then the level of O_3 is forced to be smaller in order to maintain photochemical equilibrium.

All the modelling groups appear to be internally consistent, although a more constrained test of the O_x budget at 3 mbar could verify and quantify this conclusion. The $L(O_x)$ and $L(HO_x)$ do not vary much from model to model because O_3 and H_2O have relatively small variances among the models. The $L(NO_x)$ and $L(Cl_x)$ have quite a large model to model variance. Interfamily conversion and interference as well as substantial NO_x and Cl_x level differences among the models are believed to be the causes of this large model variance.

The level of NO_x does not vary as much from model to model as does the N_2O amount, indicating that NO_x amounts are fairly robust. The $J(O_3$ tot) is the most important quantity for determining the absolute amount of O_3 at 3 mbar and has a variance of about 29%. We were surprised at the differences in $J(O_3$ tot) from model to model and encourage a more rigorous comparison of photolysis rates for a fixed atmosphere in order to investigate these differences. This more detailed photolysis intercomparison is planned as a follow-up to the two-dimensional intercomparison workshop.

Table 3-10. O_x Production and Loss Rate Comparisons

Rate	Mean	Highest Value/Lowest Value
P(tot)	4.70(11)	1.44
$L(O_x)$	3.88(10)	1.47
$L(HO_x)$	6.29(10)	1.59
$L(NO_x)$	1.16(10)	1.97
$L(Cl_x)$	5.10(10)	2.64
L(tot)	4.74(11)	1.42

*4.70(11) means 4.70×10^{11}

Table 3-11. Comparison of Ten Rates and Species at 3 mbar, Equator, in March from Five Modeling Groups

Group	P(tot) #cm^{-3} day^{-1}	L(O$_x$) #cm^{-3} day^{-1}	L(HO$_x$) #cm^{-3} day^{-1}	L(NO$_x$) #cm^{-3} day^{-1}	L(Cl$_x$) #cm^{-3} day^{-1}	J(O$_3$tot) #sec^{-1}	O$_3$ ppmv	H$_2$O ppmv	NO$_x$ ppbv	Cl$_x$ ppbv
AER	4.49(11)	8.12(10)	5.85(10)	2.30(11)	7.78(10)	1.00(-3)	5.82	4.50	17.8	2.23
GSFC1	4.72(11)	7.74(10)	6.32(10)	2.49(11)	8.73(10)	9.64(-4)	5.83	4.88	18.9	2.36
GSFC2	4.74(11)	9.14(10)	6.79(10)	2.38(11)	7.82(10)	9.57(-4)	6.04	5.03	18.2	2.01
LLNL	4.52(11)	8.10(10)	6.53(10)	2.20(11)	7.79(10)	1.12(-3)	4.85	4.95	23.0	2.26
MRI	4.61(11)	6.53(10)	7.03(10)	1.80(11)	1.26(11)	1.17(-3)	4.74	5.69	14.8	2.48

*4.49(11) means 4.49 x 10^{11}

63

Section 3.4.2 Integrated Columns of O_3, HNO_3, HCl, and HF and NO_2

Ivar Isaken

Except for HF, for which no columns were presented at the workshop, O_3, HNO_3, HCl and NO_2 columns were available from several groups. Ozone columns were available from nine (9) groups. The overall agreement among models (and with observed ozone columns) are good. This might not be surprising since total ozone columns in many cases are used to test the models, and some tuning is applied. The main feature of column ozone is reproduced in the Northern Hemisphere. Ozone maximum occurs at high latitudes during spring varying between February and May, and with a minimum in late summer and fall. Low latitude ozone levels show several variations which is in agreement with observations. The absolute values are also in fairly good agreement with observations, except for a couple of cases where ozone columns are on the high side (-10 - 20 %).

Southern Hemispheric ozone columns show considerable variations among the models. Several of the models do not predict ozone maximum at the right location and the time it is observed. Particularly, the observed low springtime values in the south polar region is not predicted in most of the models. HNO_3 is indicative of horizontal transport in the stratosphere. HNO_3 integrated columns were available for 6 models. There were marked differences among the models. Some differences were almost a factor two. All models show a marked increase toward the poles. Comparisons with observations indicate that the high column cases are closer to observations than the model estimates giving the smallest columns. However, there is one serious discrepancy between observations and all model devised columns. At high latitudes where observations show maximum values during winter, models predict a winter minimum, and a maximum during spring (1 model) or summer. One explanation which has been suggested is that models do not include heterogeneous conversion of N_2O_5 to HNO_3. This could be an important source for winter time HNO_3 as N_2O_5 is high during high latitude winter. The large differences among the models are not understood, and should be investigated.

Integrated NO_2 columns show marked variations with season and with latitudes. Maximum values occur at high latitudes during summer. At high latitude winter there is a drop in NO_2 columns poleward of approximately 60° which is in agreement with observations. Latitudinal gradients differ among the models, probably reflecting the efficiency of horizontal transport in the stratosphere. One model which calculates average diurnal values seems to give higher NO_2 columns than the other models. Using integrated diurnal average NO_2 values (one model) will probably lead to larger NO_2 columns than when noontime or daytime average values are used.

The integrated HCl columns show a large scatter. However, all models give pronounced latitudinal gradients. The differences in absolute levels are due to the effect of adopted surface level HCl. In most models, an arbitrary surface level is chosen. This leads to highly different contributions to the integrated HCl column which, in several cases, are significant. In order to make meaningful comparisons of stratospheric HCl columns, the tropospheric contribution has to be removed from the data.

In order to be able to make meaningful comparisons, the following suggestions are made: Integrated columns for HCl, NO_2 and HNO_3 are made for heights above 12 km to avoid any contribution from ground sources which leads to enhanced levels in the lower troposphere. NO_2 columns have to be calculated for the same time of day (noontime values) in all models.

The largest discrepancies among the models of integrated columns seem to be in HNO_3, which at high latitudes does not compare well with observed seasonal variations. Two groups have HF columns (not available at the workshop) which should be included in the comparisons.

Section 3.4.3 Cl$_y$ and NO$_y$

Malcolm Ko

Through photochemical reactions in the atmosphere, chlorine atoms released by photodissociation of the chlorine-containing organic molecules are transformed into HCl, ClNO$_3$, ClO, Cl, Cl$_2$ and Cl$_2$O$_2$ referred to as odd chlorine species. The concentration of total odd chlorine, [Cl$_y$], is defined as the sum of [HCl] + [ClNO$_3$] + [ClO] + [Cl] +2 [Cl$_2$O$_2$] + ... Our current understanding is that while photochemical reactions can repartition the odd chlorine species, there is no reaction occurring in the atmosphere that could chemically convert odd chlorine species to an inert form. The only mechanism for removal of Cl$_y$ is by transport to the troposphere where the soluble species such as HCl could be removed by a physical process of rain-out and wash-out. In a steady state simulation of the atmosphere, the rate of Cl$_y$ removal should be equal to the production rate from the organic molecules. The total number of chlorine atoms bound up in the organic molecules and in the Cl$_y$ species should be a constant in the stratosphere.

The recommended boundary conditions for the organic chlorine species for the 1980 atmosphere simulation are summarized in Table 3-12.

Table 3-12. Boundary Conditions for the Organic Chlorine Species for 1980

Species	Boundary condition (pptv)	Contributions to odd odd chlorine (pptv)
CH$_3$Cl	700	700
CH$_3$CCl$_3$	100	300
CCl$_4$	100	400
CFCl$_3$	170	510
CF$_2$Cl$_2$	285	570
	Total odd chlorine	2,480

If the mixing time in the troposphere is sufficiently fast, so that the mixing ratios of the organic molecules at the tropopause are the same as their boundary values, the [Cl$_y$] in the upper stratosphere where most of the source gases have dissociated should approach a uniform value of 2.5 ppbv. Note that this should hold independent of the treatment (grouping or no grouping, method of partitioning of the Cl$_y$ species) in the models.

The calculated [Cl_y] in the upper stratosphere for the models are given in Table 3-13.

Table 3-13. Calculated [Cl_y] at 50 km

Model	[Cl_y] at 50 km (ppbv)	Prescribed boundary condition
AER	2.4	yes
CAMBRAL*	2.0	*
CLKSON	2.5	no
GSFC1*	2.4	*
GSFC2	2.1	yes
LLNL*	2.4	*
MRI	2.5	yes (no CH_3Cl)+
NOCAR	2.5	no
OSLO	2.3	yes (no CH_3Cl)+
WISCAR	2.3	yes (no CH_3Cl)+

*Data from these groups were not available on the database when the table was prepared. Values estimated from graphs.
+Values for CH_3Cl not found in database

The low value for GSFC2 is due to a lower mixing ratio at the tropopause for CH_3Cl because of slow mixing in the troposphere.

The calculated vertical and latitudinal behavior of Cl_y is also useful as a diagnostic for the circulation. However, it should be noted that if one accepts the closure argument, the Cl_y behavior is a result of the combined effects of the calculated scale heights and latitudinal behaviors of different source gases. A more meaningful diagnostic could be obtained by looking at the individual source gases. A rough estimate of the circulation can be obtained by examining the vertical and latitudinal distribution of Cl_y. The vertical distributions given at the equator in Table 3-14 provides a measure of the strength of the upwelling at the tropics.

Table 3-14. Vertical distribution of calculated [Cl_y] for January

Model	Altitude(km) at which {Cl_y} is 90% of value in Table 3-13		Altitude at which {Cl_y} is 50% of value in Table 3-13	
	Equator	60° N	Equator	60° N
AER	36	26	25	18
CAMBRAL*	38	32	23	17
CLKSON	31`	31	21	21
GSFC1*	36	30	25	20
GSFC2	35	27	28	20
LLNL*	38	36	26	19
MRI	32	26	25	21
NOCAR	36	27	26	20
OSLO	31	26	25	18
WISCAR	36	30	27	24

*Data from these groups were not available on the database when the table was prepared. Values estimated from graphs.

Assuming that all models use similar boundary conditions on source gases, one can conclude from the Table 3-14 that the GSFC2 and WISCAR models have the strongest equatorial pumping in the lower stratosphere. In the upper stratosphere, the AER, GSFC2, NOCAR and WISCAR models have relatively strong pumping while those from the OSLO and MRI are considerably weaker.

The latitudinal contrast of [Cl_y] in the lower stratosphere provides a measure of the effectiveness of the competing effects of advection and eddy mixing in maintaining the slopes of the surfaces of constant mixing ratio. Table 3-15 shows that the CLKSON, MRI, CAMBRAL and WISCAR models have relatively small equator to pole contrast at 20 km.

Table 3-15.

Calculated ratio of {Cl_y} at 60°N to {Cl_y} at the Equator for January at 20 km and 30 km.

Model	20 km	30 km
AER	4.8	1.4
CAMBRAL*	3.5	1.1
CLKSON	1.0	1.0
GSFC1*	4.0	1.3
GSFC2	4.5	1.5
LLNL*	2.8	1.3
MRI	3.2	1.2
NOCAR	6.2	1.4
OSLO	5.4	1.1
WISCAR	2.1	1.3

*Data from these groups were not available on the database when the table was prepared. Values estimated from graphs.

Let us now turn to the effect of calculated Cl_y on O_3 and to what extent the difference in calculated O_3 could be explained in terms of the difference in calculated Cl_y. For the present day atmosphere, the effect of chlorine chemistry on the calculated column distribution of O_3 should be less than 10% at high latitudes. Table 3-16 shows that the calculated $[Cl_y]$ at 25 km differ typically by about 20%. The effect on explaining differences in column O_3 for the present day atmosphere should be small. However, this may be relevant in explaining the different responses of ozone in different models to chlorine perturbations.

Table 3-16. Calculated $[Cl_y]$ at 25 km (ppbv)

Model	60°N	Equator
AER	2.1	1.2
CAMBRAL*	1.9	1.6
CLKSON	1.8	1.8
GSFC1*	1.8	1.1
GSFC2	1.7	0.7
LLNL*	1.8	1.1
MRI	2.1	1.1
NOCAR	2.1	1.0
OSLO	2.0	1.2
WISCAR	1.36	0.76

*Data from these groups were not available on the database when the table was prepared. Values estimated from graphs

The impact of chlorine is more important at 40 km where the calculated Cl_y differs by 10% (see Table 3-13).

The photochemical source for NO_y in the stratosphere is from the reaction of $O(^1D)$ with N_2O. In addition to the physical removal in the troposphere, NO_y is also removed by recombination of N and NO to form molecular N_2. The vertical distribution of N as well as the reaction rate constant of N reacting with NO are a strong function of altitude in the upper stratosphere where photochemical removal is most effective. Thus, NO_y is more sensitive to transport in the upper stratosphere than Cl_y. In addition, the calculated $[NO_y]$ at the stratopause is affected by treatment of the mesospheric source of NO_y, while $[NO_y]$ in the equatorial lower stratosphere would depend on treatment of tropospheric lightning sources. All these complications make NO_y less useful as a diagnostic for circulation. In this discussion, we will concentrate on the comparison of the calculated values and the effect on O_3.

Nearly all the models calculate a maximum in $[NO_y]$ at about 40 km with the peak mixing ratio ranging from 18-23 ppbv.

Table 3-17. Calculated maximum [NO$_y$] and location of peak for January.

Model	Altitude at which maximum occurs (km)	Mixing ratio at maximum (ppbv)
AER	42	19
CAMBRAL*	42	18
CLKSON*	30	19
GSFC1*	35	22
GSFC2	40	18
LARC	39	21
LLNL*	42	22
MRI	35	17.5
NOCAR	41	23
OSLO	37	21
WISCAR*	40	22

*Data from these groups were not available on the database when the table was prepared. Values estimated from graphs.

Different models also showed significant deviation at the upper boundary of the models around 50 km.

Table 3-18. Calculated [NO$_y$] around 50 km for January

Model	Equator (ppbv)	High Latitudes (ppbv)
AER	17	10
CAMBRAL*	12	12
CLKSON*	13	10
GSFC1*	12	8
GSFC2	8	5-7
LARC	12	4
LLNL*	18	18
MRI	10	10
NOCAR	16	6-10
OSLO	14	14
WISCAR*	7	6

*Data from these groups were not available on the database when the table was prepared. Values estimated from graphs.

The calculated [NO$_y$] at 20 km at high latitudes should have a large impact on the calculated column abundance of O$_3$. Table 3-19 gives the calculated [NO$_y$] at 20 km for January for both the summer and the winter hemispheres.

Table 3-19. Calculated $[NO_y]$ at 20 km

Model	Summer 60° S (ppbv)	Winter Equator (ppbv)	Winter 60°N (ppbv)
AER	7	1.3	8
CAMBRAL*	10	2.0	10
CLKSON*	11	2.0	5
GSFC1*	5	1.0	6
GSFC2	8	0.9	4
LARC	7	2.5	--
LLNL*	10	<2	10
MRI	9	0.5	5
NOCAR	8	1.8	8
OSLO	6	1.0	10
WISCAR	5.5	<2	4

*Data from these groups were not available on the database when the table was prepared. Values estimated from graphs.

A large range of values (5-10 ppbv) is obtained among the models. In addition, some of the models (CLKSON, GSFC2, MRI, and OSLO) show large differences between the summer and the winter hemisphere.

Section 3.4.4   <u>NO_y Species</u>

Anne Douglass

Comparisons of dissociation rate calculations and transport experiments indicate that there are substantial differences among these models. In spite of these sources of variance, comparison of ratios of family members provides a measure of the overall consistency of the models. The interchange reactions among the odd nitrogen species ($NO_y = NO + NO_2 + NO_3 + HNO_3 + HO_2NO_2 + 2\ N_2O_5 + ClONO_2 + HNO_2$) are rapid compared to the net production and loss of NO_y. These interchange reactions are affected both directly and indirectly by model quantities including dissociation rates, the concentrations of species such as odd hydrogen species which are in photochemical equilibrium, and the concentrations of long lived (transported) species.

The ratio $(NO + NO_2)/NO_y$, whether daytime average or noontime concentrations are used to formulate the ratios, indicates the fraction of total NO_y that participates in the catalytic cycles that destroy ozone. For January current atmosphere values, these ratios show remarkable agreement. For all models, the ratio is greater than 0.9 at 40 km. At 35 km, the high and low values of the ratio are all in the range 0.75 to 0.90. At 30 km, the model ratios are in the range 0.45 to 0.60. Above about 28 km, the ratio is smaller at the winter pole than at the summer pole. In the lower stratosphere there is some similarity among the major structures.

Similar agreement is seen for the ratio HNO_3/NO_2. Although the high latitude, lower stratospheric lifetime of HNO_3 is long, through much of the stratosphere its concentration is controlled by photochemical processes. The photochemical equilibrium ratio is given by

$$\frac{k_1\ [OH]\ [M]}{k_2\ [OH] + k_3\ [O] + J} \quad\text{approx.} = \quad \frac{k_1\ [OH]\ [M]}{J}$$

where k_1 is the rate for $NO_2 + OH + M$, k_2 for $OH + HNO_3$, k_3 for $O + HNO_3$ and J is the dissociation rate for HNO_3; J dominates the other two loss processes. The consistency of the values of this ratio among the models is a measure of the consistency of the ratio of the OH concentration to the dissociation rate for HNO_3.

Section 3.4.5 Cl$_y$ in the Current Atmosphere

Richard Eckman

For the purposes of the intercomparison, the abundances of chlorine source gases in the present day atmosphere were fixed to yield a total inorganic chlorine level of 2.48 ppbv in the stratosphere. The uniform level of Cl$_y$ removes some of the uncertainty associated with the comparison of the models. Interchange between family members determines the efficiency at which the odd chlorine family destroys odd oxygen, primarily through reactions involving Cl with O$_3$ and ClO with O in the upper stratosphere. This intercomparison focused on several ratios of chlorine species and the absolute abundances of certain family members (ClO, ClNO$_3$, HOCl, and HCl) to ascertain the areas of disagreement among the models.

Cl and ClO rapidly interchange throughout much of the stratosphere and their relative abundance is

$$\frac{[Cl]}{[ClO]} = \frac{k_1[O] + k_2[NO] + J_{ClO}}{k_3[O_3] + k_4[NO]}$$

The dependence of the ratio on NO and the photodissociation of ClO are secondary to the reactions involving O and O$_3$. Hence, this ratio should reflect closely the ratio of oxygen and ozone examined in the next section.

Among the models examined in this study, a substantial degree of consistency is seen among the results of this ratio with discrepancies generally less than 20%, at least above 30 km. The comparison is impaired however by steep gradients in the ratio in the 40-50 km range.

HCl in the stratosphere acts as a reservoir for odd chlorine by effectively sequestering Cl$_y$ in a form that removes it from participating in odd oxygen destruction. HCl can be formed by reaction of Cl with CH$_4$ and also HO$_2$. In the lower stratosphere, reaction of Cl with CH$_2$O can also be important. Lesser sources involve reactions with H$_2$O$_2$ and H$_2$. The primary source of destruction is by reaction with OH. The ratio of ClO to HCl will clearly show the importance of the differences in model-calculated CH$_4$, a long-lived gas, and the odd hydrogen family (through its dependence on OH and HO$_2$). Agreement among the models in the upper stratosphere (30-50 km) is, again, reasonable but with somewhat more spread than in the case of Cl/ClO. Indeed, the ratio is in a sense a convolution of both the Cl/HCl and Cl/ClO relative abundances. Therefore, discrepancies in the Cl/ClO ratio will be reflected in the ClO/HCl comparison. It is difficult to ascribe the differences to any one factor without a critical intercomparison of the other species mentioned above which was not possible during the time frame of the workshop.

Recent airborne measurements by Brune et al. (Polar Ozone Workshop Abstracts, NASA Conference Pub. 10014, 189-190, 1988) at northern high latitudes (~60°N) in the winter lower stratosphere reveal elevated levels of ClO in the 55 pptv range. Table 3-20 shows the ClO mixing ratio calculated by the models. These values are at least a factor of three below the measured value and thus cannot account for the enhancement in ClO.

Table 3-20.   Calculated ClO at 50 mb, 60°N latitude

Model	ClO (pptv)
NOCAR	10
AER	20
GSFC2	2-10
MRI	10
DUPONT	5
LLNL	16

Section 3.4.6 O_x and HO_x Partitioning, H_2O_2, CH_2O

Paul Guthrie

O/O_3

The odd-oxygen partitioning between atomic oxygen and ozone depends primarily on the model treatment of ozone photolysis. A comparison of the O/O_3 ratio among models thus gives us information about differences in the ways the models handle radiative transfer in the near UV, and about the ways the models compute photolysis rates, including seasonal variation and diurnal (or other temporal) averaging effects. Where ozone photolysis becomes small (i.e. at large optical depths), the ratio becomes sensitive to processes involving other chemical families (e.g. NO_2 photolysis)

The spread in model distributions of O/O_3 is perhaps somewhat surprising. The two GSFC models use essentially the same photolysis calculation, and as might be expected, have similar distributions of O/O_3. They differ more below 20 km where the differences in the treatment of other chemical families becomes more important. Using GSFC2 arbitrarily for comparison purposes, the overall span in O/O_3 values for all models is roughly plus 100% (AER) to minus 50% (WISCAR, LLNL) based on the December distributions.

There are substantial differences in the seasonality of the ratio. LLNL, WISCAR, and OSLO are the most strongly seasonal (steepest winter/summer slope), while CAMBRAL and LARC show minimal latitudinal variation, at least in December. Most models show a monotonic increase in the ratio at summer high latitudes for a constant altitude, but some (CAMBRAL, AER, LARC) have a tropical maximum at least at some altitudes.

There are also differences in the "shape" of the altitude variations of the ratio. For example, GSFC2, OSLO and MRI all have similar values at 20 and 30 km, but at 40 km MRI is perhaps a factor of three larger than GSFC2, while OSLO is perhaps 50% smaller than GSFC2.

O_3

There are some notable differences in the O_3 distributions among the models. Differences in the curvature of isopleths (especially the upward-poleward extension in high latitudes in the winter hemisphere) appear to be related to the eddy diffusion coefficients used. There is a spread of ~20% between the peak mixing ratios obtained by various models. There is also a substantial difference in the mixing ratios obtained by the various models in the 10-20 km altitude region. This is presumably related to the relative strengths of the upward advection and downward diffusion in the lower stratosphere and the troposphere.

OH/HO_2

Based solely on a comparison of the OH/HO_2 ratio among models, there is less disagreement for these species than for most others in this intercomparison. That is perhaps to be expected since transport plays essentially no role in determining this partitioning, at least in the middle and upper stratosphere. All models show a value of 1.0 for this ratio between 37 and 40 km. There is a slight offset (perhaps 1-2 km) in this between the models which compute temperature and those which specify it, consistent with the small temperature differences seen at these altitudes. The ratio decreases with decreasing altitude, reaching a minimum of about 0.1 somewhere between 20 and 30 km in most models, with the exception of LARC. Since the ratio becomes sensitive to the CH_4 concentration in this altitude range, and thus to the already established differences in transport among models, greater variance is probably to be expected in this region. The LARC exception is presumably due to the specification of the CH_4 distribution in that

74

model.

There is some indication that differences in chemical schemes may affect the OH/HO_2 ratio at 40 km near the polar terminator. One group of models (WISCAR, GSFC1, OSLO) shows substantial structure in the ratio in this region, while a second group (AER, NOCAR, GSFC2, LARC) shows much flatter contours. The NOCAR model has unique structure in the ratio at 16 km which is presumably a reflection of the lower boundary treatment.

$\underline{HO_2}$

There is a disagreement among models as to HO_2 distribution in the upper stratosphere and lower mesosphere. In CAMBRAL the mixing ratio slope decreases with altitude, in effect, creating a broad maximum at the model top. AER has an approximately constant slope to a maximum value of 450 pptv. The other models have constant or slightly increasing slope to maximum values of 550 pptv or greater. The different mixing ratio values at the model tops may simply reflect different maximum altitudes, but slope differences are probably related to differences in HO_x production rates, given the similarity of OH/HO_2 ratios.

$\underline{H_2O_2, CH_2O}$

For H_2O_2 all models show a similar distribution in the stratosphere with a broad tropical maximum reaching a peak mixing ratio of about 0.2-0.4 ppbv (CAMBRAL is slightly below 0.2 and MRI is slightly above 0.4) at 30 km. There is a minimum at around 16 km which varies substantially among models, presumably due to differences in transport and tropospheric removal. GSFC1 appears to be somewhat anomalous in this, using a much faster removal rate for H_2O_2 than the other models. There is also some indication that the H_2O_2 distribution may not have converged completely in GSFC1.

The CH_2O distributions are also similar with a tropical mixing ratio maximum at about 40 km and another at the ground. MRI has a notably smaller mixing ratio peak in the stratosphere than other models (< 0.1 ppbv) while LARC has the largest (> .25 ppbv). The other models show peak values of about .15 - .25 ppbv.

Section 3.4.7 Distribution and Lifetimes of Source Gases

Malcolm Ko and Donald Fisher

Source gases with lifetimes longer than one year are uniformly distributed in the troposphere where mixing is very efficient. Gases transported to the stratosphere are removed by photochemical reactions. The calculated distributions of the source gases in the stratosphere is a good indication of the efficiency of transport to maintain the concentration against photochemical loss. The behavior of the simulated distributions of the trace gases from the different models are consistent with the strengths of their circulations as discussed in Section 3.3.2. Models with stronger circulations would have higher concentrations in the stratosphere. The lifetimes of the trace gases as calculated by some of the models are given in Table 3-21.

Table 3-21. Model Calculated Lifetimes (years) of Source Gases*

Trace Gas	AER	GSFC2	LLNL
N_2O	114	168	130
CCl_4	40	52	52
F-11	46	60	60
F-12	95	132	121

* Some of the values given in this table are taken from simulations performed for the UNEP/WMO report and do not correspond exactly to the distributions given in Chapter 6, however the difference should be small.

The lifetimes for the trace gases given in Table 3-21 are determined by removal in the stratosphere. As expected, models with strong circulations that predict higher concentrations in the stratosphere give shorter lifetimes. Lifetimes for the species such as CH_4 and CH_3CCl_3 are determined by removal in the troposphere through reaction with OH. Calculated values from the models will depend on the treatment of tropospheric chemistry in predicting OH in the models.

Section 3.5   Perturbed Atmospheres

Donald J. Wuebbles
Matthew H. Hitchman

For the workshop, each of the modeling groups was asked to examine their calculated effects on ozone from four steady-state scenarios for perturbed concentrations of CFCs, CO_2, and other trace gases. In each scenario, the change in ozone is determined relative to a "1980" atmosphere, as indicated in Table 3-22. The four perturbation scenarios, as defined in Table 3-22, are:

A = All trace gases perturbed (including approximately 8 ppbv Cl_y, 2 x CO_2, 2 x CH_4,
    1.2 x N_2O);
B = 2 x CO_2 only;
C= CFC perturbation only; and
D = all gases perturbed except CO_2

Many of the groups brought results to the meeting and the calculated changes in stratospheric ozone and temperature were compared. However, there was insufficient time to make detailed comparison of the results, and at this time, many of the differences in the results from different models remain unresolved. In order to not mislead the reader, we have chosen not to present any of the individual graphs for the perturbation results in ozone of the different groups until a more detailed comparison of two-dimensional (and three-dimensional) model results for the perturbed atmosphere can be done at a later time. However, we will provide an overview of the results.

Table 3-22.   Reference and perturbed atmospheres

| | Tropospheric Mixing Ratios | | Scenario | | | |
	"1980"	"20xx"	A	B	C	D
CO_2*	340 ppm	680 ppm	•	•		
N_2O	300 ppb	360 ppb	•			•
CH_4	1.6 ppm	3.2 ppm	•			•
H_2O(at tropopause)*	3.0 ppm	unchanged				
CO	100 ppb	unchanged				
CH_3Cl	700 ppt	unchanged				
CH_3CCl_3	100 ppt	unchanged				
CCl_4	100 ppt	unchanged				
$CFCl_3$	170 ppt	800 ppt	•		•	•
CF_2Cl_2	285 ppt	2200 ppt	•		•	•
CH_3Br	20 ppt	40 ppt	•			

* To be included where possible/applicable.

Table 3-23 describes which modeling groups provided calculations for the perturbed atmosphere scenarios, and, in a rough sense, gives an indication of those models that determine interactive changes in temperature and/or circulation, as well as determining the chemical effects on ozone. There were five groups that both submitted perturbation results and that have the

77

capability for treating interactive temperature and/or circulation changes. For example, the LLNL model has fixed circulation and eddies for perturbation calculations, but allows the changes in net heating rates to affect stratospheric temperatures. Other models, such as NOCAR and WISCAR, are attempting to include fully interactive radiation, circulation, and wave-driven eddies in their calculations (the approaches used in different models to determine these interactions vary widely, reflecting the significant uncertainties in attempting to make current models fully interactive).

Table 3-23. Modeling groups represented in the perturbations calculations discussed, and their capability at the time of the workshop for determining interactive heating rates (ΔQ), temperatures (ΔT), and circulation $(\Delta \chi)$ changes. The degree at which various models are "interactive" in determining these changes varies, and is not represented by this table.

Model representatives	Interactive $\Delta Q, \Delta T, \Delta \chi$	Ran perturbations
AER	No	Yes
DUPONT	No	Yes
GSFC2	No	Yes
MRI	No	No
MPIC	No	No
OSLO	No	Yes
LLNL	$\Delta Q, \Delta T$	Yes
CLKSON	$\Delta Q, \Delta \chi$	No
CALJPL	$\Delta Q, \Delta \chi$	No
AERI	$\Delta Q, \Delta T, \Delta \chi$	Yes
CAMBRAL	$\Delta Q, \Delta T, \Delta \chi$	No
NOCAR	$\Delta Q, \Delta T, \Delta \chi$	Yes
WISCAR	$\Delta Q, \Delta T, \Delta \chi$	Yes
GSFC1	$\Delta Q, \Delta T, \Delta \chi$	Yes

As we will discuss below, there was a wide variation in the calculated changes in total ozone among models for the four cases. Tables 3-24 through 3-26 present the results from several of the models compared at the meeting for the calculated changes in total ozone in the tropics and at the poles for scenarios C, B, and A, respectively. For the CFC-only scenario, the models generally agreed well in their calculated changes in total ozone for the tropics. However, two models got much larger changes in ozone at the poles than the other three models. Very large differences were found among models for the doubled CO_2 scenario. Part of this difference, as seen in Table 3-25, is related to whether tropospheric temperatures were assumed to have changed for the perturbed atmosphere. The altitude at which lower stratospheric temperatures are first allowed to be perturbed in the model also appears to affect the change in total ozone determined. Given the significant differences in results among models for cases B and C, it is not surprising that there are substantial differences in the calculated changes in total ozone for case A, where all of the gases are perturbed together.

Table 3-24. Comparison of calculated change in total ozone from five models for scenario C (Cl_y only perturbation). The models are listed randomly.

Model	Δ Total O_3 (%) Tropics	Δ Total O_3 (%) Pole
A	-2	- 6
B	-3	- 6
C	-4	-12
D	-4	- 6
E	-4	-16

Table 3-25. Calculated changes in total ozone for scenario B (2 x CO_2) from three models. Models are listed randomly. Also shown is whether tropospheric temperatures were assumed to be changed for this scenario.

Model	ΔT in troposphere	ΔTotal O_3 (%) Tropics	Pole
F	No	+1.5	+ 5.6
F	Yes	+1.2	+ 2.8
G	No	+4.0	+10.0
H	No	+1.8	+ 7.5

Table 3-26. Calculated changes in total ozone for scenario A from three models. Models are listed randomly.

Model	ΔTotal O_3 (%) Tropics	Pole
I	-0.4	+2.0
J	+3.0	+7.0
K	0	-2.5

In contrast, reasonably good agreement was found among models for the temperature perturbations calculated for the scenarios. Regarding the effects on dynamics, there is agreement between the AERI and WISCAR models regarding the feedback of gravity wave drag, wherein a weakened pole-to-pole circulation above 30 km occurs as a result of the latitudinal variations in projected temperature decreases in cases A-D. The WISCAR model reports a modest Rossby wave feedback in cases where CO_2 doubling alters lower stratospheric temperatures somewhat. Initial diagnosis suggests a delayed spring polar ozone maximum. Changes in temperature and net heating rates calculated for the four scenarios from available models are presented in the database summary of plots. A more detailed comparison of model results for perturbed atmospheres is to be done for the International Ozone Scientific Assessment report next year. That report will also

need to examine what effect including heterogeneous chemistry in these models, such as for the conversion of N_2O_5 to HNO_3 at winter polar latitudes or the reaction of chlorinated molecules on particle surfaces, has on perturbation calculations. Future comparisons of perturbed atmospheres in two- and three- dimensional models will require much more detailed analysis of the differing approaches used to treat radiative and dynamical, as well as chemical interactions. We need to determine how these interactions are affected in perturbed atmospheres.

Section 3.6 References

Allen, M., and J. E. Frederick, Effective photodissociation cross sections for molecular oxygen and nitric oxide in the Schumann-Runge bands, J. Atmos. Sci., 39, 2066-2075, 1982.

Johnston, H. S., and J. Podolske, Interpretations of stratospheric photochemistry, Rev. Geophys. and Space Phy., 16, 491-519, 1978.

Nicolet, M., and W. Peetermans, Atmospheric absorption in the O_2 Schumann-Runge band spectral region and photodissociation in the stratosphere and mesosphere, Planet. Space Sci., 28, 85-103, 1980.

TRACER EXPERIMENT Y
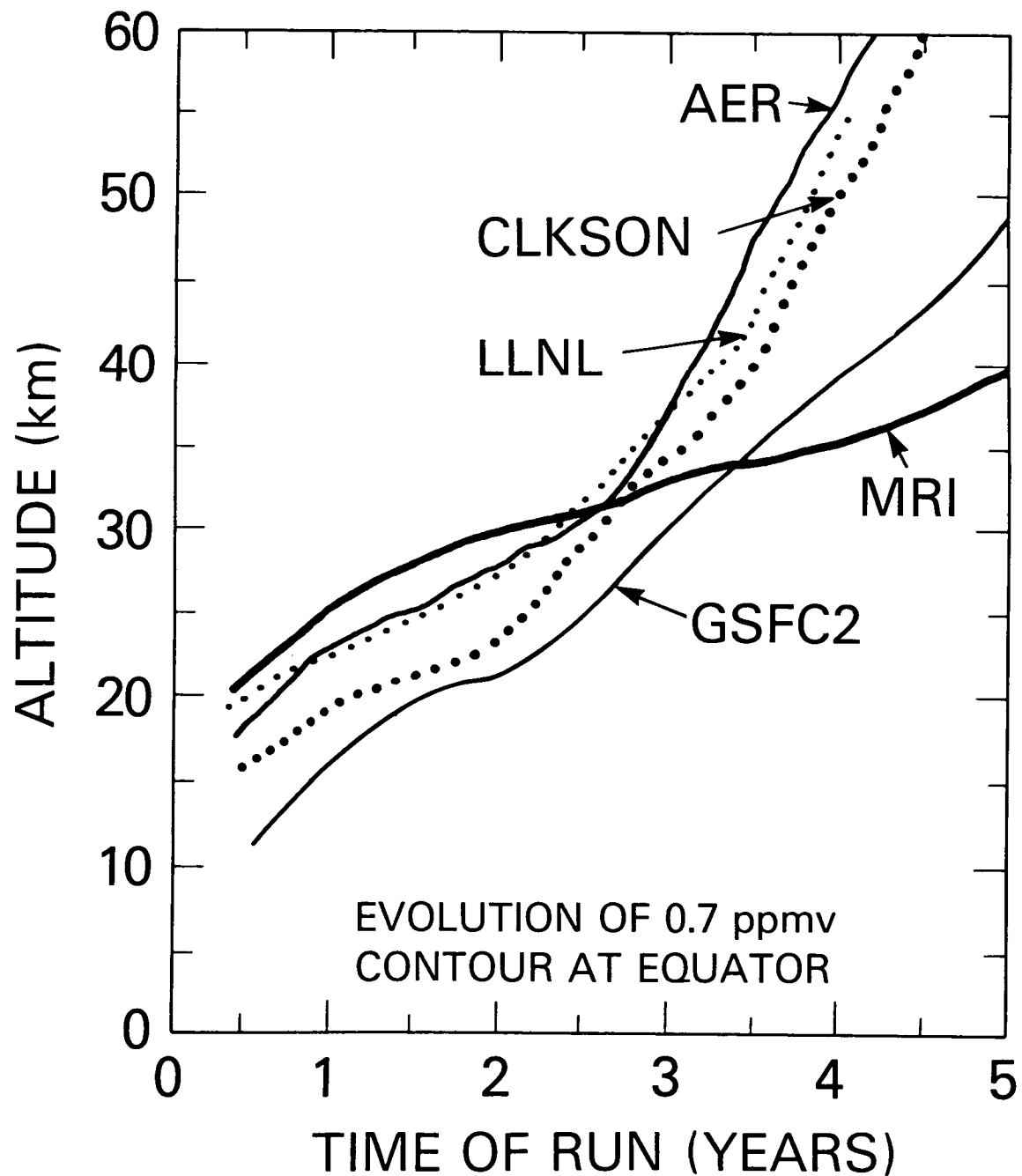
Figure 3-1. Time evolution of the 0.7 ppmv contour at the equator is shown for models AER, CLKSON, GSFC2, LLNL, and MRI.
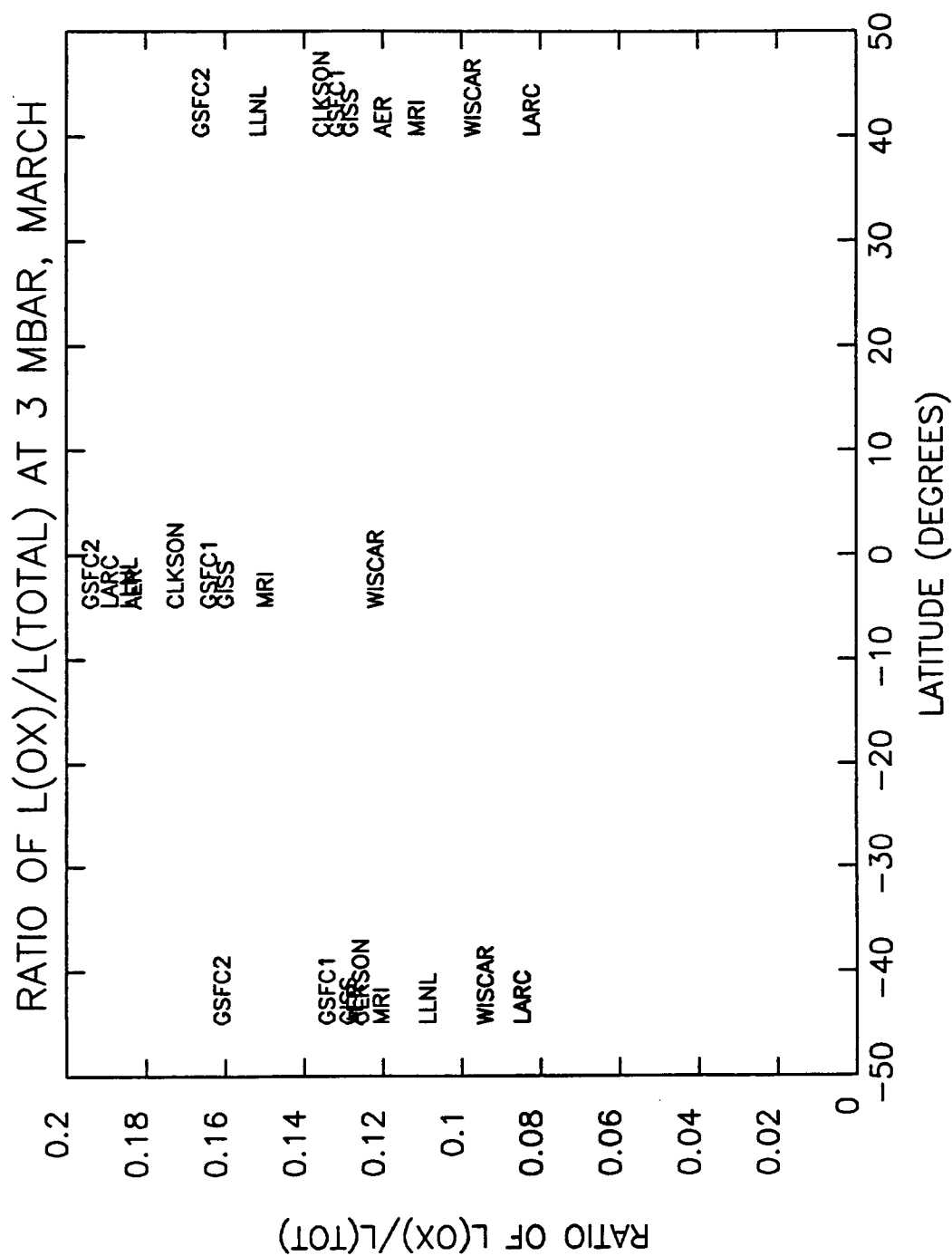
Figure 3-2. The relative fraction of odd oxygen (ozone) loss in a family at 3 mbar (40 km) for latitudes 45°S, 0°, and +45°N degrees is given for a) L(O$_x$)/L(tot).
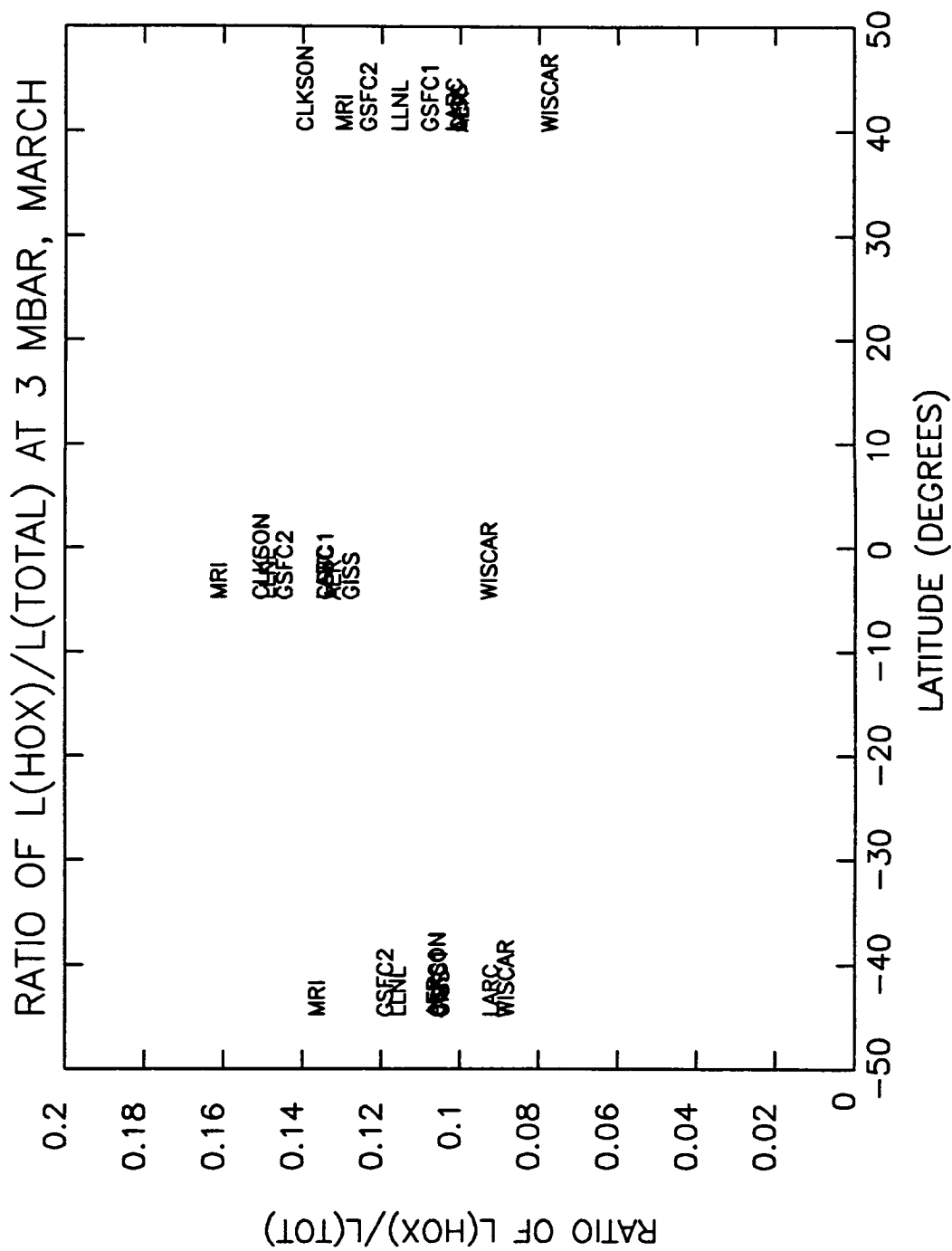
Figure 3-2. The relative fraction of odd oxygen (ozone) loss in a family at 3 mbar (40 km) for latitudes 45°S, 0°, and +45°N degrees is given for b) L(HO$_x$)/L (tot).
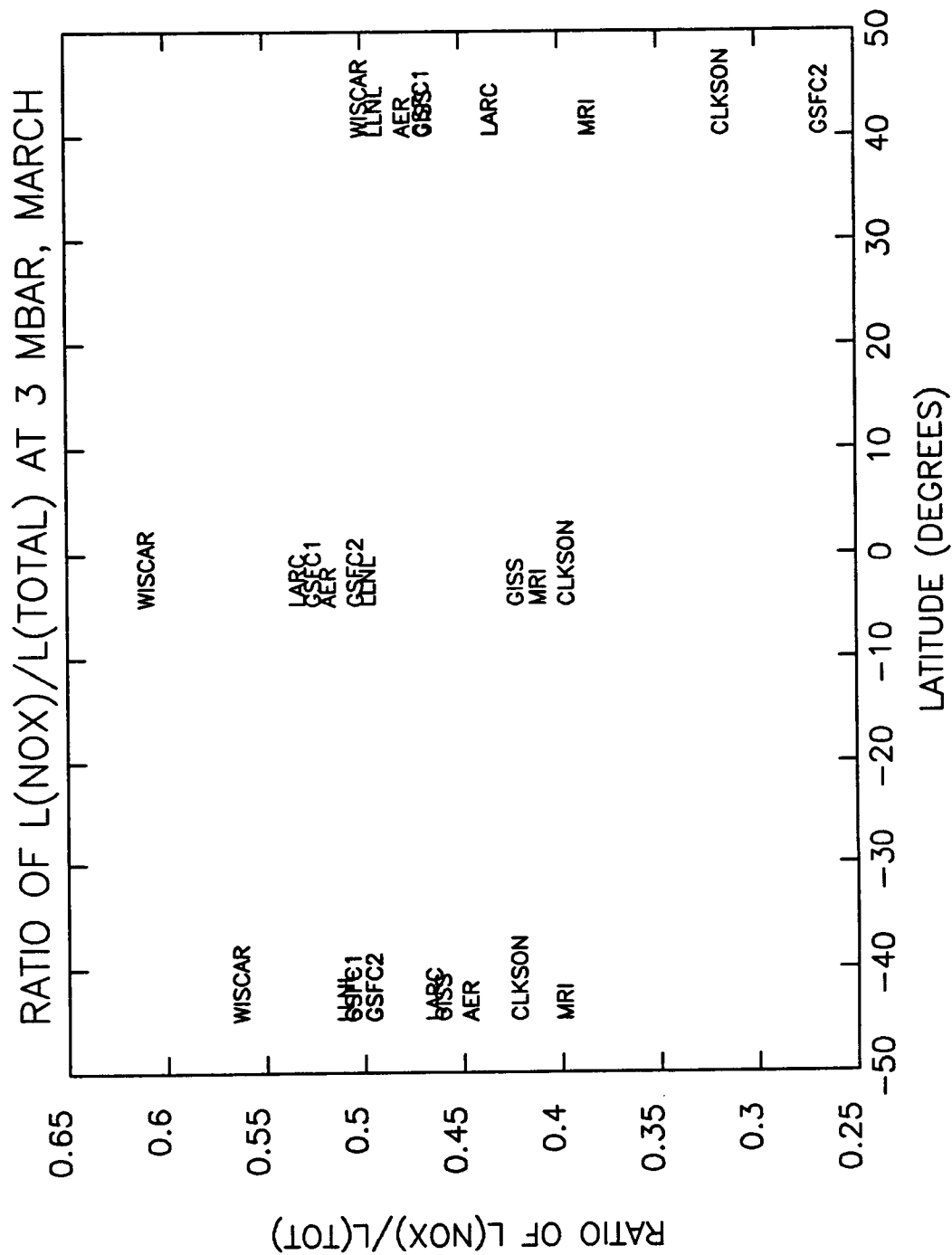
Figure 3-2. The relative fraction of odd oxygen (ozone) loss in a family at 3 mbar (40 km) for latitudes 45°S, 0°, and +45°N degrees is given for c) $L(NO_x)/L(tot)$.
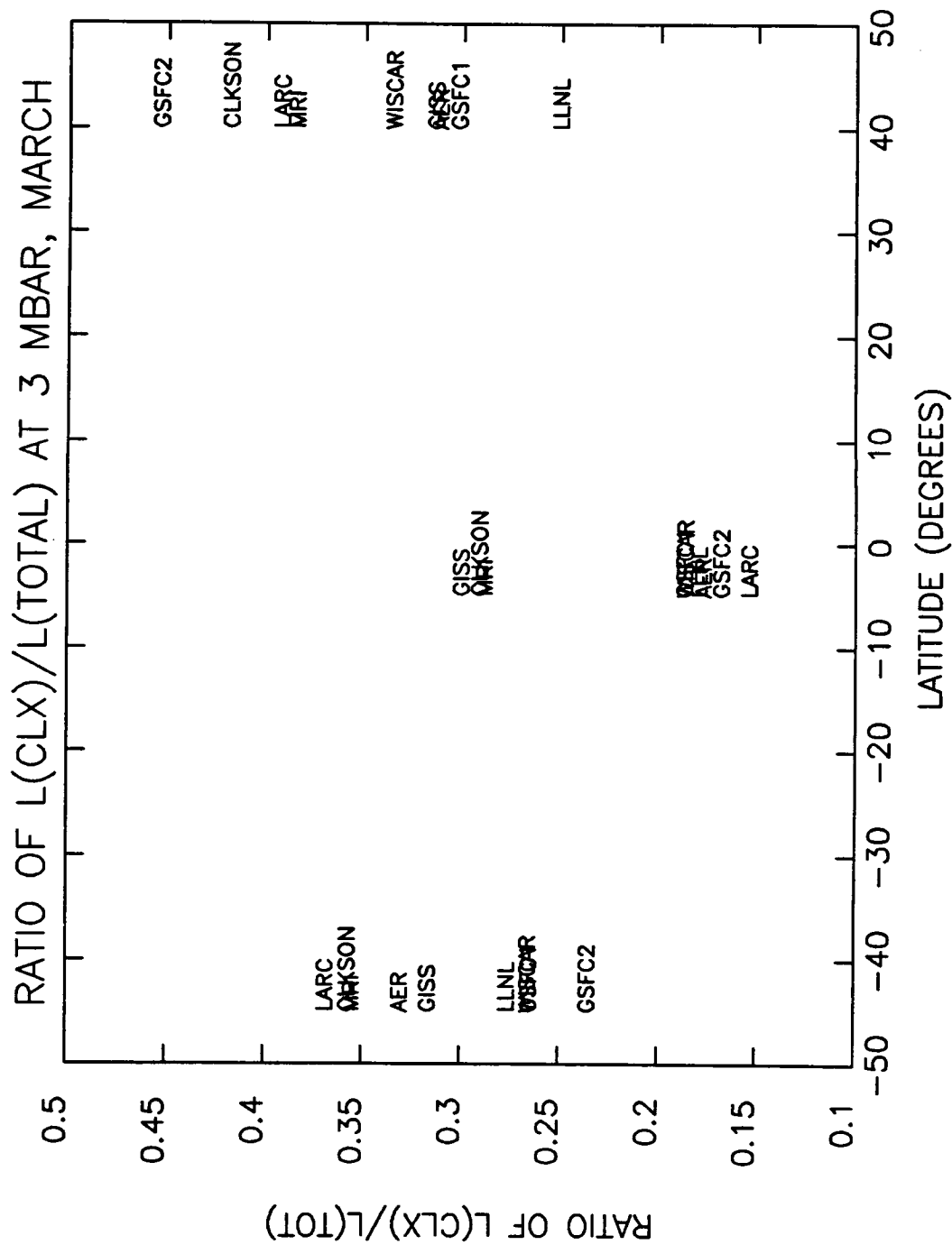
85

RATIO OF L(CLX)/L(TOTAL) AT 3 MBAR, MARCH

Figure 3-2. The relative fraction of odd oxygen (ozone) loss in a family at 3 mbar (40 km) for latitudes 45°S, 0°, and +45°N degrees is given for d) L (Cl$_x$)/L(tot).

86
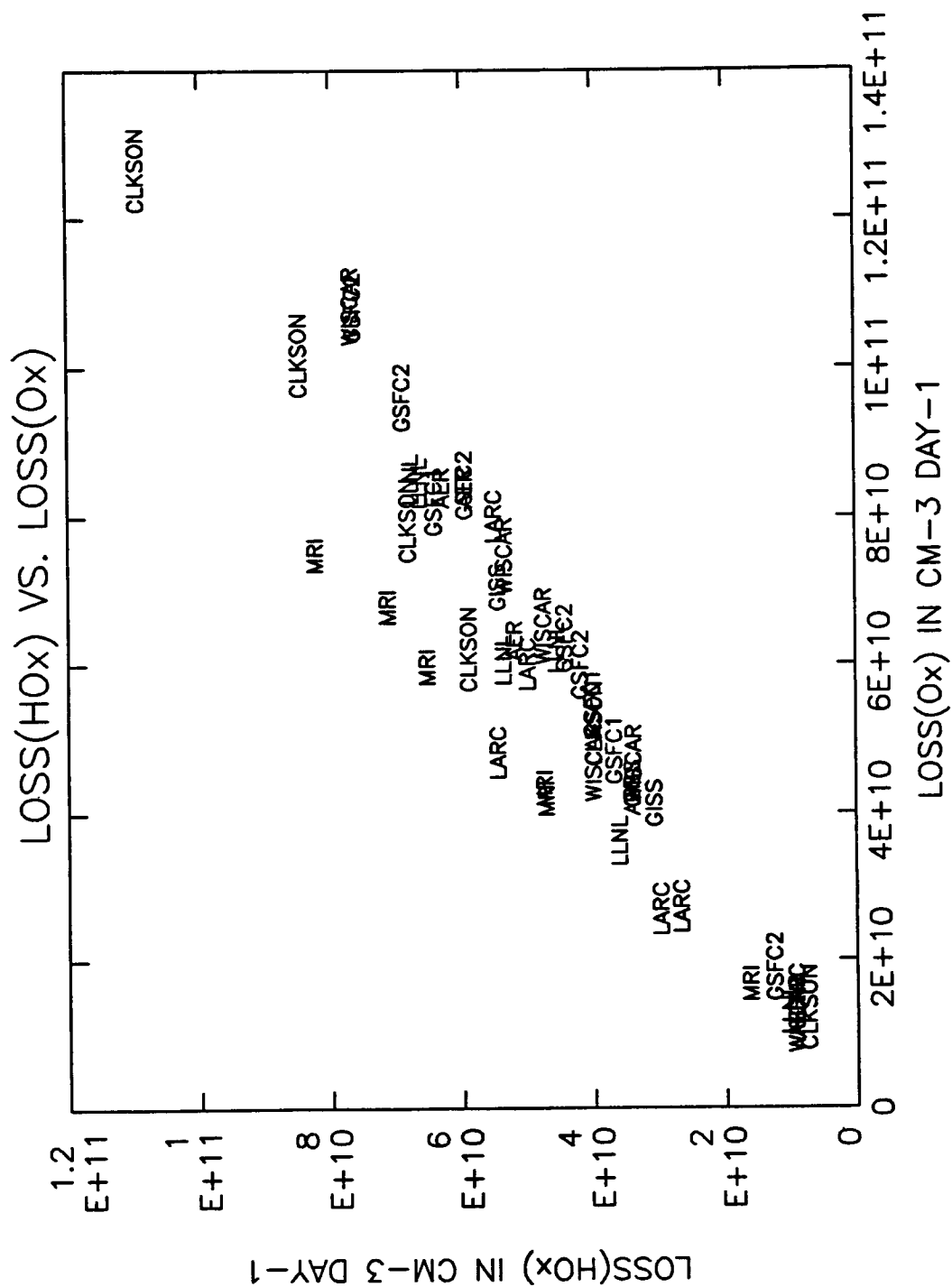
Figures 3-3. The loss of odd oxygen due to O_x, $L(O_x)$, as a function of the loss of the odd oxygen due to HO_x, $L(HO_x)$; all points given for level 3 mbar (40 km).
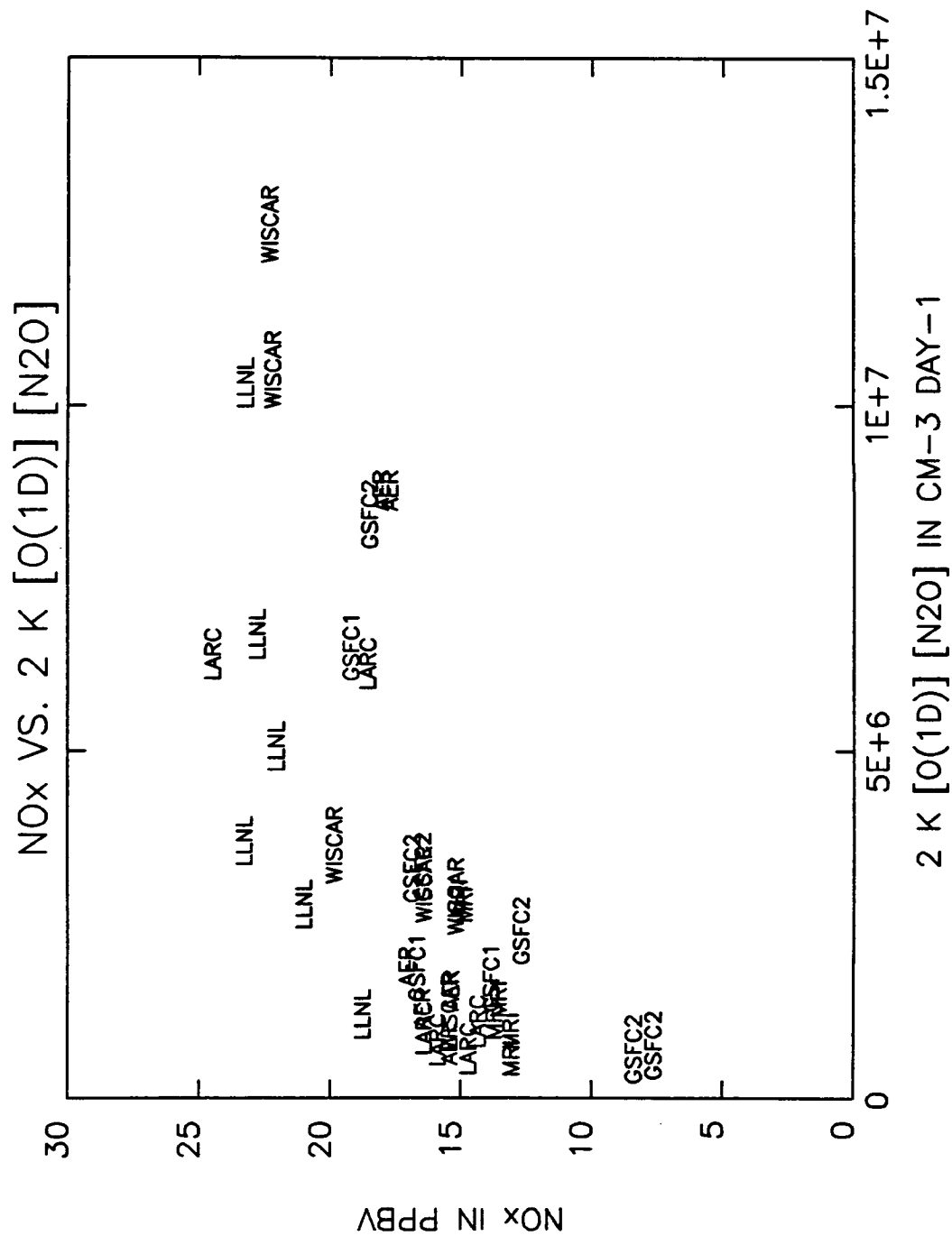
Figure 3-4. The production of odd nitrogen, $2 k[O(^1D)][N_2O]$, as a function of NO_x at 3 mbar (40 km).

Section 3.7 Appendix: Comparison Of Thermal Infrared Cooling Rates

Report was prepared after the September 11-16, 1988 2-D Workshop

Dave Crisp

Objectives:

This test was designed to compare the thermal infrared cooling rate algorithms that are currently being used in 2-D chemical tracer transport models. Thermal cooling rates play an important role in these models since the advective component of the 2-D transport circulation is usually approximated by the diabatic circulation, which is derived from the difference between the solar heating rates and the thermal cooling rates. Accurate methods for finding thermal cooling rates are essential in this application because the solar heating and thermal cooling rates often differ by only a few percent. This is particularly true in the middle and lower stratosphere, where the trace gas distribution is largely determined by transport. At these levels, 10% errors in either the solar heating or thermal cooling will often produce 100 % errors in the computed diabatic circulation.

Earlier comparisons of radiative algorithms have revealed large differences in thermal cooling rates for identical input model atmospheres. To help determine the causes of these differences, thermal fluxes and cooling rates were computed separately for model atmospheres that included only H_2O, CO_2, or O_3, as well as for an atmosphere that included all three gases. Cooling rates obtained from an accurate line-by-line calculation were used as an absolute standard in these tests.

Model Atmospheres Used:

Atmospheric pressures and temperatures from the McClatchey et al. (1971) "Midlatitude Summer" sounding were used for all tests in this comparison. H_2O and O_3 mixing ratios were also derived from that source. Two different CO_2 mixing ratio profiles were used, including a "1980 atmosphere" (300 ppmv) and a "doubled CO_2" (600 ppmv) case. These quantities were specified at the middle of 123 layers between the surface and approximately 100 km.

Standard Line-by-Line Cooling Rates:

Fluxes and cooling rates obtained from the GFDL line-by-line model (Fels and Schwarzkopf, 1981; Schwarzkopf and Fels, 1985) were used as the standard "exact" results in this comparison. These results were chosen because they were available, and because they were included and validated as part of the ICRCCM comparison study (Luther and Fouquart, 1984).

Spectral Intervals:

Spectrally-resolved fluxes and heating/cooling rates were requested for the following spectral intervals to facilitate the diagnosis of differences among models:

test	gas	interval (cm^{-1})	bands included

1) H$_2$O: 0 - 1650   6.3, rotation, continuum: ICRCCM case 20.
2) CO$_2$:   450 - 900   15 micron band only: ICRCCM case 9 and 10.
3) O$_3$:   0 - 1350   9.6 and 14 micron bands: ICRCCM case 23.
4) ALL: 0 - 1650   All bands of all gases: ICRCCM case 27.

The Models Used:

Eight groups participated in the revised thermal cooling rate comparison:

1) GFDL   (S. B. Fels, M.D. Schwarzkopf, S. Freidenreich, GFDL/NOAA)
2) Caltech   (D. Crisp, Jet Propulsion Laboratory/Caltech)
3) Clarkson   (K.K. Tung, E. Olaguer, and H. Yang, Clarkson).
4) Goddard   (J. Rosenfield, NASA Goddard Space Flight Center)
5) LLNL   (K. Grant, Lawrence Livermore National Laboratory)
6) Leningrad   (I. Karol, Main Geophysical Observatory, Leningrad)
7) Mainz   (C. Bruehl, Max-Planck Institute for Chemistry, Mainz)
8) Oslo   (F. Stordal, Institute for Geophysics, Oslo)

No two groups used the same algorithm, and there are vast differences in computational efficiency and accuracy of the methods evaluated here. Each model is briefly outlined below.

1. The GFDL Line-By-Line Model:

Fels and Schwarzkopf (1981) describe the GFDL line-by-line model as a "substantially-modified version of a code provided by Drayson" (Drayson, 1967). This classical line-by-line model employs an explicit integration over the spectrum. The spectral resolution is variable, with finer spacing near line cores (< 0.001 cm^{-1}). A Voigt line shape is used. The sub-Lorentzian behavior of the far wings of CO$_2$ lines is modeled by cutting lines off 3 cm^{-1} from the line center, and renormalizing the line-shape function. The far wings of H$_2$O and O$_3$ lines are assumed to have Lorentzian profiles. These lines are cut off 10 cm^{-1} from the line center. They use an explicit integration over optical path in the transmission calculation. Four-point Gaussian quadrature is used to perform the integration over zenith angle in the thermal flux equation. These procedures avoid errors produced by the commonly-used Curtis-Godsen and Diffusivity-Factor approximations, respectively.

The GFDL model atmospheres are divided into 123 (case 4), 108 (cases 2 and 3) or 52 (Case 1) levels. The model atmospheres used in cases 2 through 4 extend from the surface to 0.001 mbar (approximately 93 km). The model atmosphere used in case 1 (H$_2$O) extends from the surface to 10 mbar. Vertical levels are equally spaced in log(pressure), but different spacings are used at pressures above and below 100 mbar. At pressures greater than 100 mbar, the vertical resolution is approximately 1/2 km. At lower pressures, the vertical resolution is approximately 1 km. Much finer resolution is used to compute the transmission between nearby layers. Cooling rates were interpolated (or extrapolated) to the 123 level grid for this comparison. These line-by-line computations are based on the 1982 AFGL line catalog (Rothman et al. 1983). Further details of this model are documented in Fels and Schwarzkopf (1981) and Schwarzkopf and Fels (1985).

The GFDL line-by-line cooling rates were provided on a 1600 BPI magnetic tape by Stuart Freidenreich of GFDL. These cooling rates were resolved into 10 cm^{-1} spectral intervals for 18 different model atmospheres. A more complete description of this tape is given in the appendix. Copies of the tape can be obtained from Stuart Freidenreich. The cases and spectral regions chosen here are listed above.

We have discovered two errors in the description of the GFDL H_2O cooling rates that were distributed for this test. First, the GFDL H_2O cooling rates extend only from the surface to 10 mbar. Cooling rates above this level were extrapolated, and not used in this intercomparison. Second, The GFDL model did not include H_2O continuum absorption case 1. This accounts for the large discrepancies in the tropospheric H_2O cooling rates reported by all groups.

2. Caltech:

The Caltech algorithm accounts for extinction by gases, clouds, and aerosols. A Voigt quasi-random model is used to find the line absorption by all gases in all spectral regions (see Wyatt et al. 1962 for a general description of these models). The principal approximation used in this narrow band model is that absorption line positions are uncorrelated within narrow spectral regions (5 cm^{-1} for these runs). This simplification usually improves the computational speed by about a factor of 300 over the line-by-line model. Unlike the commonly-used Goody (1952) and Malkmus (1967) random models, the quasi-random model uses a Voigt line shape and an accurate description of the line strength distribution in each narrow spectral region. A direct integration over inhomogeneous optical paths is used to avoid errors introduced by the Curtis-Godsen approximation. The transmission calculation for each spectral interval explicitly accounts for absorption by the far wings of spectral lines with centers outside of that interval. The standard version of this model employs a diffusivity factor approximation instead of an explicit integration over zenith angle in the thermal flux calculation.

The method described by Roberts et al. (1976) is used to account for water vapor continuum absorption. The absorption by cloud and aerosol particles in partially-cloudy model atmospheres can also be included, but multiple scattering is ignored. Only clear (cloud and aerosol free) model atmospheres were used in this comparison. The 123-level ICRCCM model atmosphere was interpolated to a standard 75 layer grid (0 to 65 km) for these tests. Line parameters were obtained from the 1986 version of the AFGL line catalog (Rothman et al. 1987).

3. Clarkson:

The Clarkson model uses different broad-band formulations to find the absorption by CO_2, H_2O and O_3. The CO_2 algorithm is based on an emissivity parameterization developed by Ou and Liou (1983). This model uses a polynomial fit to the Fels and Schwarzkopf (1981) line-by-line transmission data.

The ozone model is similar to the method originally described by Rosenfield et al. (1987). A single-interval Malkmus (1967) random model is used to find the transmission in the 9.6 micron band. Doppler and Voigt effects are included by a simple modification to the Lorentz halfwidth (Fels, 1979). A Curtis Matrix approach is used to find the cooling rates by this band. The integration over angle in the thermal flux equation is replaced by the diffusivity-factor approximation.

Water vapor absorption in the 6.3 micron and rotation bands is computed with a method similar to the broad-band model for CO_2 described by Ramanathan (1976). Within the CO_2 15 micron band, water vapor absorption is found using a single-interval Goody (1952) random model. The method described by Roberts et al., (1976) is used to include the effects of water vapor continuum absorption at wavelengths between 8 and 12 microns. This model can also account for partially-overlapped black clouds. The 123-level ICRCCM grid was used in these calculations.

4. Goddard:

The Goddard model uses different algorithms for finding CO_2, H_2O and O_3 transmission (Rosenfield et al., 1987; Rosenfield, 1989). The CO_2 broad-band transmission algorithm uses precomputed transmissions for a standard atmosphere temperature profile. The temperature dependence of the transmission is treated by a linear expansion method. The standard atmosphere transmission and the linear expansion coefficients are computed by line-by-line calculations at 0.002 cm^{-1} resolution. The CO_2 mixing ratio is fixed at 330 ppmv. The line-by-line calculations, which employ a full Voigt profile and

explicit integration over zenith angle, are described in Chou and Kouvaris (1976). The cooling rates computed by this line-by-line code differ from those given in Schwarzkopf and Fels (1985), especially in the 10 mbar region. The Chou and Kouvaris calculations give about 0.4 K/day less cooling than the Schwarzkopf and Fels model. These differences have been attributed to different treatments of the line cutoff. When Chou and Kouvaris increase the limits of the line cutoff, their line-by-line calculations agree much better with those given in Fels and Schwarzkopf (1985).

The O_3 transmission algorithm has just been updated (Rosenfield, 1989). The new model divides the 9.6 micron band into band-center and band-wing components, and uses a model with the functional form of the Goody (1952) random model to find the transmission in each region. Band parameters for each region are derived by fitting line-by-line calculations which incorporate Voigt line shape effects.

The broad-band model of Chou (1984) is used to find transmission in water vapor bands. The method of Roberts et al. (1976) is used to include water vapor continuum absorption. Both the ozone and water vapor models use a method similar to the Curtis-Godsen approximation to compute transmission along inhomogeneous atmospheric optical paths. For the ozone model, a diffusivity factor approximation is used to parameterize the effects of integration over zenith angle in the thermal flux calculation. Line parameters for all gases were obtained from the 1982 version of the AFGL line catalog (Rothman et al. 1983). The 123-layer ICRCCM model atmosphere was interpolated to the standard Goddard grid, with 45 levels between the surface and 90 km.

5. LLNL:

The radiative transfer code used at Lawrence Livermore National laboratory is based on broad-band parameterizations for CO_2, O_3 and H_2O that were originally compiled and documented by Harshvardhan et al. (1987). CO_2 transmission in the 15 micron is computed using a modified version of the broad-band model of Chou and Peng (1983). This algorithm uses a "far-wing" model at levels below the upper stratosphere, and a different parameterization at higher levels. A single-interval Malkmus (1967) random model (Rodgers, 1968) is used to find the transmission in the 9.6 micron ozone band. Water vapor absorption in the 6.3 micron and rotation bands is computed using the broad-band model (Chou, 1984). The method described by Roberts et al. (1976) is used to compute the water vapor continuum absorption. This algorithm can also account for the extinction by absorbing clouds in a partially-cloudy atmosphere.

6. Leningrad:

The radiative transfer model used at the Main Geophysical Laboratory in Leningrad is based on the Goody (1952) random model. The thermal infrared spectrum is divided into 17 spectral intervals. The band parameters in each interval are based on the 1975 AFGL line catalog. The Curtis-Godsen approximation is used to account for variations in the absorber amount, pressure and temperature along inhomogeneous atmospheric optical paths. The diffusivity factor approximation is used instead of an explicit integration over zenith angle in the thermal flux equation. Their model atmosphere uses 2 km vertical resolution between the surface and 60 km.

7. Mainz:

The model used at the Max Planck Institute for Chemistry is described in Bruehl and Crutzen (1988). CO_2 absorption is derived from a simplified version of the Kiehl and Ramanathan (1983) model. They divide the CO_2 15 micron band into 52 sub-bands. The effects of partial overlap between these sub-bands is included only in the calculation of transmission to space (i.e. the flux at the top of the atmosphere). Total overlap is assumed for all other paths. The Ramanathan and Dickinson (1979) model is used to find O_3 transmission. This model has been modified to include contributions from hot and isotopic bands. H_2O absorption in the rotation band is computed using the method of Ramanathan

92

(1976). The Roberts et al. (1976) model is used to find the H_2O continuum absorption. Heating and cooling rates are computed directly from analytic derivatives of the absorption functions. This model uses 86 levels between the surface and 64 km. Cooling rates were reported only at levels in the stratosphere and lower mesosphere. An approximate method is used to include the effects of tropospheric clouds on the upwelling flux at the base of the model.

8. Oslo:

The Oslo model is described in Stordal (1988). The model for CO_2 and O_3 is based on the wide-band model described by Ramanathan (1976) and Kiehl and Ramanathan (1983). This model explicitly accounts for partially-overlapped hot and isotopic bands, as well as the fundamental band. The Ramanathan and Downey (1986) non-isothermal emissivity formulation is used for H_2O. A method similar to the Curtis-Godsen approximation is used to accommodate the effects of changes in the absorber amount, temperature and pressure along inhomogeneous atmospheric optical paths. A diffusivity approximation is used to parameterize the integration over angle in the thermal flux equation.

RESULTS:

Contributions to the radiative cooling by H_2O, CO_2, and O_3 are shown along with the combined effects of all three gases in Figures 3-5(a - h). H_2O is the principal absorber at tropospheric levels. The standard case chosen from the GFDL tape did not include continuum absorption. This accounts for most of the H_2O cooling rate differences at levels near the surface. The remaining differences among the models are caused primarily by inadequate vertical resolution in the troposphere.

All three gases contribute significantly to the radiative forcing at levels between 50 and 250 mbar. At these levels, CO_2 and H_2O cooling must balance the solar and thermal heating by O_3. Ozone thermal heating (negative cooling) is produced as upwelling thermal flux from the warm surface and is absorbed by the ozone layer in the cool lower stratosphere. At levels near the stratopause, CO_2 produces up to 80% of the cooling. O_3 is the next most important absorbing gas, producing about 25% as much cooling as CO_2 at these levels. H_2O cooling rates rarely exceed 1 K/Day in the stratosphere. (Note: GFDL cooling rates for H_2O were not available for pressures less than 10 mbar.)

At most stratospheric levels, cooling rates for doubled CO_2 (600 ppmv) are comparable to the combined cooling rates from CO_2, H_2O, and O_3 in the present atmosphere (300 ppmv CO_2). Differences between the cooling rates obtained by each model and the GFDL line-by-line model are shown in Figures 3-6 and 3-7. The largest cooling rate differences (K/Day) occur at levels near 1 mbar, where the cooling rates are largest. Most models underestimate the GFDL line-by-line cooling rates at these levels [Figure 3-6 (a - g)].

The largest relative differences (Figure 3-7) occur at levels where the GFDL cooling rates approach zero. The large O_3 cooling rate differences at levels near 10 mbar in Figure 3-7 are caused by very small differences in the altitude where the O_3 cooling rate crosses through zero. Such apparent errors are not a cause for concern in 2-D modeling.

1. Caltech:

The Caltech model never differs from the GFDL model by more than 0.7 K/Day, and the differences are always smaller than 0.02 K/day at levels in the middle and lower stratosphere. Errors in the total cooling rate never exceed 8% at stratospheric levels. CO_2 cooling rates are overestimated by almost 10% at levels near 5 mbar, but these errors are partially offset by a small underestimate of the O_3 cooling rates at this level. CO_2 cooling rate errors at levels between 1 and 10 mbar are primarily a consequence of the relatively course spectral resolution used in this comparison. These errors can be reduced by 60% if the

spectral resolution is increased from 5 cm⁻¹ to 1 cm⁻¹, but we cannot afford to run the model at this higher resolution on the existing MicroVAX computer. The diffusivity factor approximation contributes about 25% of the error for the present atmosphere (300 ppmv) and about 40% of the error for the doubled CO_2 case. The Caltech model underestimates the H_2O and O_3 cooling rates by up to 10% (0.02 K/Day) at some stratospheric levels, but these errors rarely contribute more than 1% to the total error budget.

2. Clarkson:

The Clarkson model underestimates the cooling rates by approximately 20% throughout the stratosphere. Most of this disagreement is caused by an underestimate of the CO_2 cooling rates. Systematic errors of this magnitude were somewhat surprising, since the Clarkson CO_2 model is based on a polynomial fit to the GFDL line-by-line data (Fels and Schwarzkopf, 1981). These cooling rate differences are partially offset in the middle and lower stratosphere by 20 to 30% overestimates of the H_2O cooling. Ozone cooling rates are overestimated at pressures greater than 1 mbar, and underestimated at lower pressures.

3. Goddard:

The Goddard model also underestimates the GFDL cooling at most stratospheric levels, but these models generally differ by more than 1 K/Day. The largest cooling rate differences (20%) occur in the lower stratosphere. CO_2 cooling rate differences of 10 to 20% account for most of the disagreement between the Goddard CO_2 model and GFDL. The Goddard broad-band model is based on the Chou Kouvaris line-by-line model, which also differs from the GFDL model by about this amount. This disagreement has been attributed primarily to differences between the treatments of the far wings of CO_2 lines. The new O_3 cooling rate model (Rosenfield 1989) performs very well, rarely producing errors larger than 5%. The H_2O algorithm underestimates the cooling by this gas by 10 to 30% (0.1 K/Day) at levels in the middle and lower stratosphere. Errors in the total cooling rate by all three gases are somewhat larger than the sum of the errors contributed by each component because ozone cooling in the 14 micron band was neglected in the total cooling rate calculation. This weak ozone band contributes up to 0.22 K/Day at some stratospheric levels.

4. LLNL:

The LLNL model underestimates the total cooling by 10 to 40% at stratospheric levels. Much of this disagreement can be attributed to underestimates of the CO_2 cooling rates. These errors are partially offset at most levels by 20 to 40% overestimates of ozone cooling rates. Errors in the total cooling by all gases are much larger than the sum of the errors by each component because cooling by the 14 micron ozone band was neglected in the total cooling calculation.

5. Leningrad:

The Leningrad model underestimates the cooling by up to 30% (0.1 K/Day) in the lower stratosphere, overestimates the cooling by about 10% (1 K/Day) at the 3 mbar level, and underestimates the cooling by up to 40% (5 K/Day) at the 1 mbar level. Crisp et al. (1986) show that these differences are primarily a consequence of the shortcomings of the CO_2 line strength distribution and line shape assumed in the Goody random model.

6. Mainz:

The performance of the Mainz model is similar to that of the Leningrad model, even though they use very different algorithms. This model overestimates the cooling by 10 to 15% at levels between 2 and 100 mbar, and underestimates the cooling by up to 25% above this level. Most of this discrepancy can be attributed CO_2 cooling rate differences. Crisp et al. (1986) show that CO_2 cooling rate errors of this magnitude can be produced as a consequence of the neglect of Voigt line shape effects in the Kiehl and Ramanathan (1983) model. Further, CO_2 cooling is underestimated because of the assumption of total overlap between the CO_2 subbands.

7. Oslo:

The Oslo model underestimates the cooling by 10 to 40% throughout the stratosphere. Differences between this model and the Mainz model are somewhat surprising, since both are based on the Ramanathan (1976) algorithm. At pressures less than 5 mbar, much of the disagreement can be attributed to an underestimate of the CO_2 cooling rates. A large underestimate of the ozone cooling rates at pressures greater than 5 mbar accounts for most of the errors at those levels.

CONCLUSIONS:

Several factors contribute to the errors encountered in this investigation. With the exception of the line-by-line model, all of the models employ simplifying assumptions that place fundamental limits on their accuracy and range of validity. For example, all 2-D modeling groups use the diffusivity factor approximation. This approximation produces little error in tropospheric H_2O and CO_2 cooling rates, but can produce significant errors (>10%) in CO_2 and O_3 cooling rates at the stratopause. Much larger errors in CO_2 cooling rates (50%) are produced at these levels if Voigt line-shape effects are not accurately modeled. The Curtis-Godson approximation produces little error in CO_2 or H_2O cooling rates, but can cause 5 to 10% O_3 cooling rate errors in the middle and lower stratosphere. The broad-band convolution of the transmission and the Plank function in the thermal flux equation can produce errors that range from 10 to 50% throughout the stratosphere. Such errors are largely avoided in narrow-band models, but these methods are too computationally expensive for use in applications where cooling rates must be recomputed often. All models suffer from fundamental uncertainties in shapes and strengths of spectral lines.

Thermal flux algorithms currently being used in 2-D tracer transport models produce cooling rates that differ by as much as 40% for the same input model atmosphere. Disagreements of this magnitude are important since the thermal cooling rates must be subtracted from the almost-equal solar heating rates to derive the net radiative heating rates and the 2-D model diabatic circulation. For much of the annual cycle, the net radiative heating rates are comparable in magnitude to the cooling rate differences described above.

Many of the models (Clarkson, Goddard, LLNL and Oslo) underestimate the cooling rates in the middle and lower stratosphere. The consequences of these errors for the net heating rates and the diabatic circulation will depend on their meridional structure, which was not tested here. Other models underestimate the cooling at levels near 1 mbar (Clarkson, Leningrad, Mainz and Oslo). Such errors pose potential problems for future interactive ozone assessment studies, since they could produce artificially-high temperatures and increased O_3 destruction at these levels. These concerns suggest that a great deal of work is needed to improve the performance of thermal cooling rate algorithms used in 2-D tracer transport models.

REFERENCES CITED:

Bruehl, C. and P.J. Crutzen, "Scenarios of possible changes in atmospheric temperatures and ozone concentrations due to man's activities, estimated from a one-dimensional coupled photochemical climate model," J. Climate Dynam., 2, 173-203, 1988.

Chou, M.D., "Broadband water vapor transmission functions for atmospheric IR flux computations," J. Atmos. Sci., 41, 1775-1778, 1984.

Chou, M.D. and A. Arking, "Computation of infrared cooling rates in the water vapor bands, J. Atmos. Sci., 37, 856-867, 1980.

Chou, M.D. and L. Kouvaris, "Monochromatic calculations of atmospheric radiative transfer due to molecular line absorption," J. Geophys. Res., 91, 4047-4055, 1986.

Chou, M.D. and L. Peng, "A parameterization of the absorption in the 15 micron CO_2 spectral region with applications to climate sensitivity studies," J. Atmos. Sci., 40, 2183-2192, 1983.

Crisp, D., S.B. Fels, and M.D. Schwarzkopf, "Approximate methods for finding CO_2 15 micron band transmission in planetary atmospheres," J. Geophys. Res., 91, 11851-11866, 1986.

Drayson, S.R. "Atmospheric transmission in the CO_2 bands between 12 microns and 18 microns," Applied Optics, 5, 385-391, 1967.

Fels, S.B., "Simple strategies for inclusion of Voigt effects in infrared cooling rate calculations," Applied Optics , 18, 2634-2637, 1979.

Fels, S.B. and M.D. Schwarzkopf, "An efficient, accurate algorithm for calculation CO_2 15 micron cooling rates," J. Geophys. Res., 86, 1205-1232, 1981.

Goody, R.M., "A statistical model for water-vapour absorption," Quart. J. Roy. Meteor. Soc., 78, band 165-169, 1952.

Harshvardhan, R. Davies, D.A. Randall, and T.G. Corsetti, "A fast radiation parameterization for atmospheric circulation models," J. Geophys. Res., 92, 1009-1016, 1987.

Kiehl, J.T., and V. Ramanathan, "CO_2 radiative parameterizations used in climate models: Comparison with narrow band models and with laboratory data," J. Geophys. Res., 88, 5191-5202, 1983.

Luther, F.M., and Y. Fouquart, "The intercomparison of radiation codes in climate models (ICRCCM) ," WMO Rep. WCP-93, 37 pp., World Meteorological Organization, Geneva, Switzerland, 1984.

McClatchey, R.A., R.W. Fenn, J.E.A. Selby, F.E. Voltz, and J. S. Garing, "Optical properties of the atmosphere (Revised)," Rep. AFCRL-71-0279, 85pp, Air Force Cambridge Research Laboratory, Bedford, MA, 1971.

Ou, S.S. and K.N. Liou, "Parameterization of carbon dioxide 15 micron band absorption and emission, " J. Geophys. Res., 88, 5203-5207, 1983.

Ramanathan, V. "Radiative transfer within the Earth's troposphere and stratosphere, a simplified radiative-convective model," J. Atmos. Sci., 33, 1330-1346, 1976.

Ramanathan, V. and R.E. Dickinson, "The role of stratospheric ozone in the zonal and seasonal ' radiative energy balance of the earth-troposphere system," J. Atmos. Sci., 36, 1084-1104, 1979.

Ramanathan, V. and P. Downey, "A non-isothermal emissivity and absorptivity formulation for water vapor, " J. Geophys. Res., 91, 8649-8666, 1986.

Roberts, R.E., J.E.A. Selby, and L.M. Biberman, "Infrared continuum absorption by atmospheric water vapor in the 8-12 micron window," Applied Optics, 15, 2085-2090, 1976.

Rodgers, C.D., "Some extensions and applications of the new random band model for molecular band transmission ," Quart. J. Roy. Meteor. Soc., 94, 99-102, 1968.

Rosenfield, J.E., M.R. Schoeberl, and M.A. Geller, "A computation of the stratospheric diabatic circulation with an accurate radiative transfer model," J. Atmos. Sci., 44, 859-876, 1987.

Rosenfield, J.E., "A simple parameterization of ozone infrared absorption for atmospheric heating rate calculations ," submitted to J. Geophys. Res., 1989.

Rothman, L.S., R.R. Gamache, A. Barbe, A. Goldman, J.R. Gillis, L.R. Brown, R.A. Toth, J.M. Flaud, and C. Camy-Peyret, "AFGL atmospheric line parameters compilation: 1982 edition," Applied Optics, 22, 2247-2256, 1983.

Rothman, L.S., R.R. Gamache, L.R. Brown, R.A. Toth, H.M. Pickett, R.L. Poynter, J.M. Flaud, C. Camy-Peyrey , A. Barbe, N. Husson, C.P. Rinsland, and M.A.H. Smith, "The HITRAN Database : 1986 edition," Applied Optics, 26, 4058-4096, 1987.

Schwarzkopf, M.D. and S.B. Fels, "Improvements to the algorithm for computing CO_2 transmissivities and cooling rates," J. Geophys. Res., 90, 10541-10550, 1985.

Stordal, F. "A wide band model for transfer of infrared radiation: Altitudinal, latitudinal and yearly variation of cooling rates in the troposphere and stratosphere," Institute Report Series, No. 68, Institutt for Geofysikk, Universitetet I Oslo, 1988.

Wyatt, P.J., V. R. Stull, and G.N. Plass, "Quasi-Random Model of band absorption," J. Opt. Soc. Amer., 32, 1209-1217, 1962.
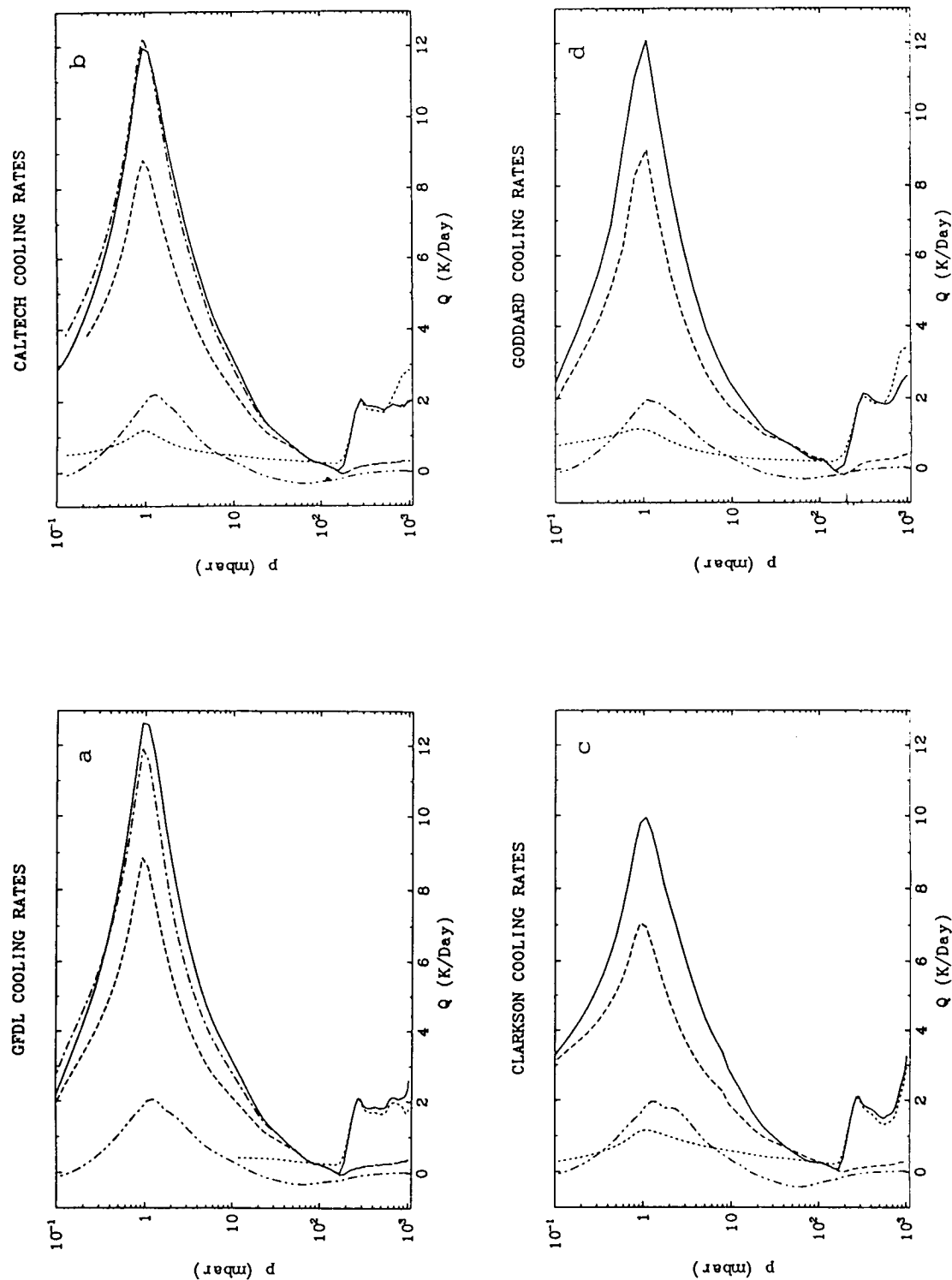
Figure 3-5. Cooling rates for H_2O (dotted), CO_2 (long dash), doubled CO_2 (dash-dot) and O_3 (dash-dot-dot) are shown along with the total cooling rate by all gases (solid) for the: (a) GFDL, (b) Caltech, (c) Clarkson, (d) Goddard, (e) LLNL, (f) Leningrad, (g) Mainz, and (f) Oslo models. All models except the GFDL model include water vapor continuum absorption at tropospheric levels. Water vapor cooling rates for the GFDL model were available only for pressures greater than 10 mbar. No tropospheric cooling rates were given for the Mainz model.
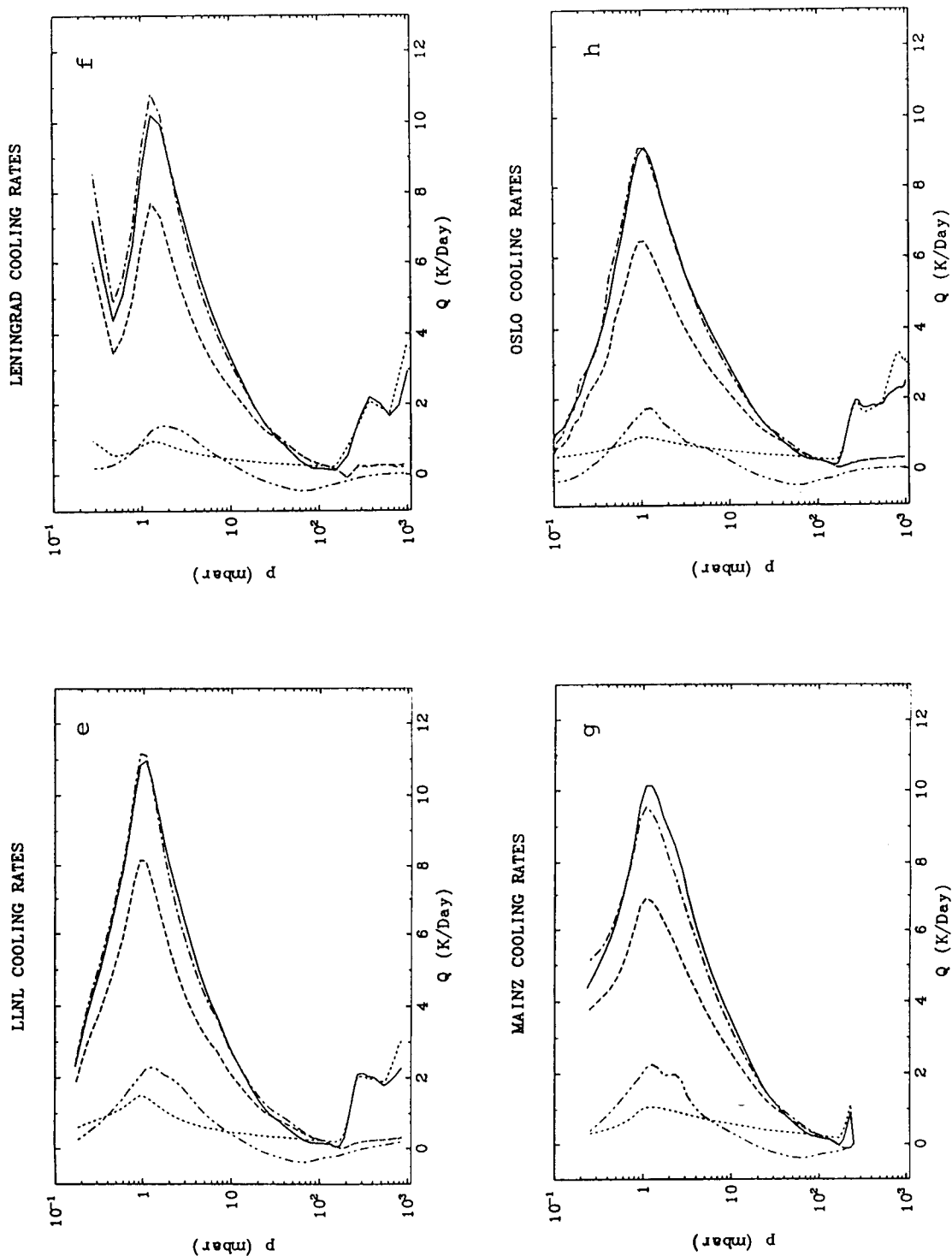
Figure 3-5 (continued). Cooling rates for H_2O (dotted), CO_2 (long dash), doubled CO_2 (dash-dot) and O_3 (dash-dot-dot) are shown along with the total cooling rate by all gases (solid) for the: (a) GFDL, (b) Caltech, (c) Clarkson, (d) Goddard, (e) LLNL, (f) Leningrad, (g) Mainz, and (f) Oslo models. All models except the GFDL model include water vapor continuum absorption at tropospheric levels. Water vapor cooling rates for the GFDL model were available only for pressures greater than 10 mbar. No tropospheric cooling rates were given for the Mainz model.

99
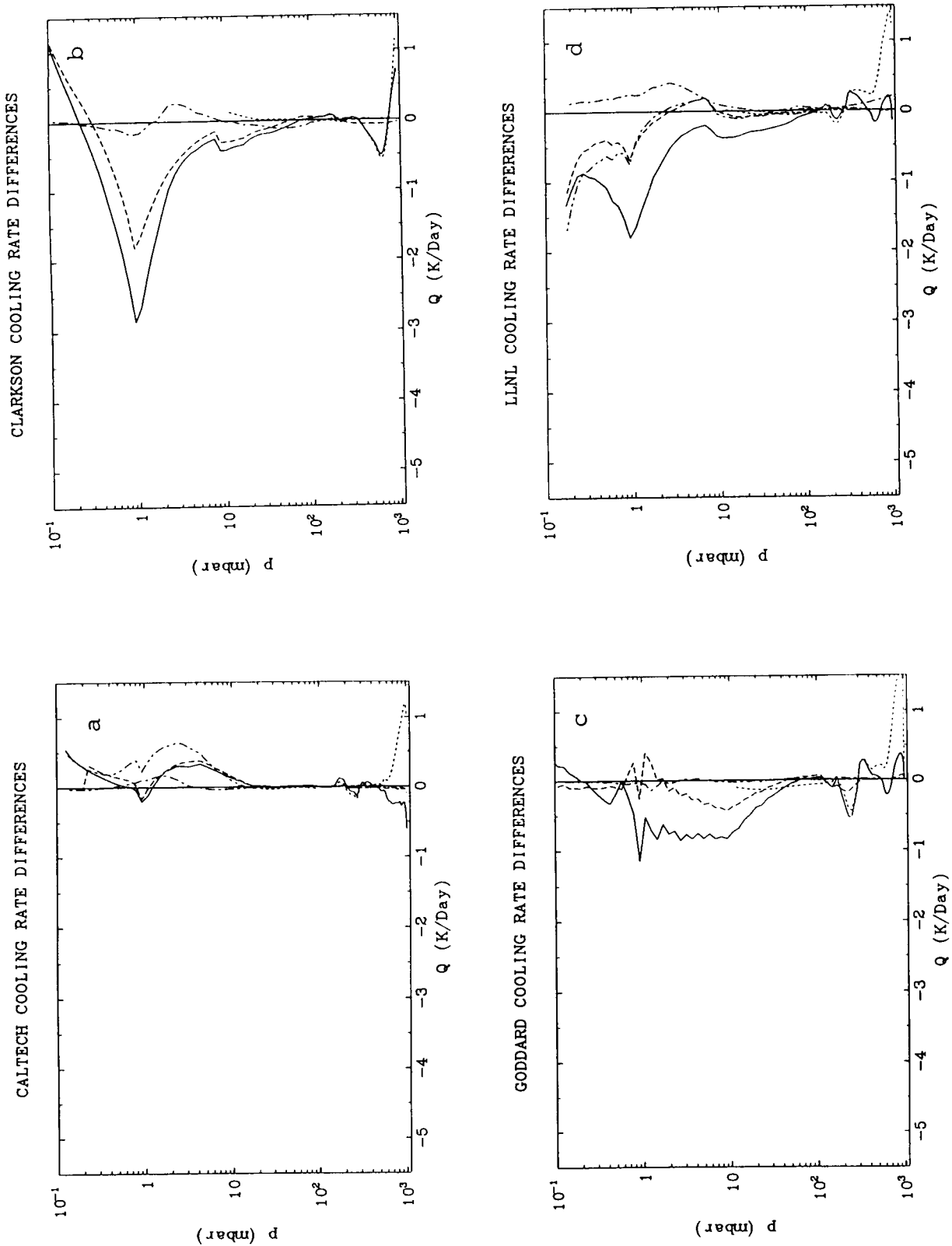
Figure 3-6. Differences between the cooling rates obtained from each model and those from the GFDL line-by-line model are shown for H_2O (dotted), CO_2 (330 ppmv, long dash; 660 ppmv, dash-dot-dot), O_3 (dash-dot), and the total cooling rate by all three gases (solid).

100
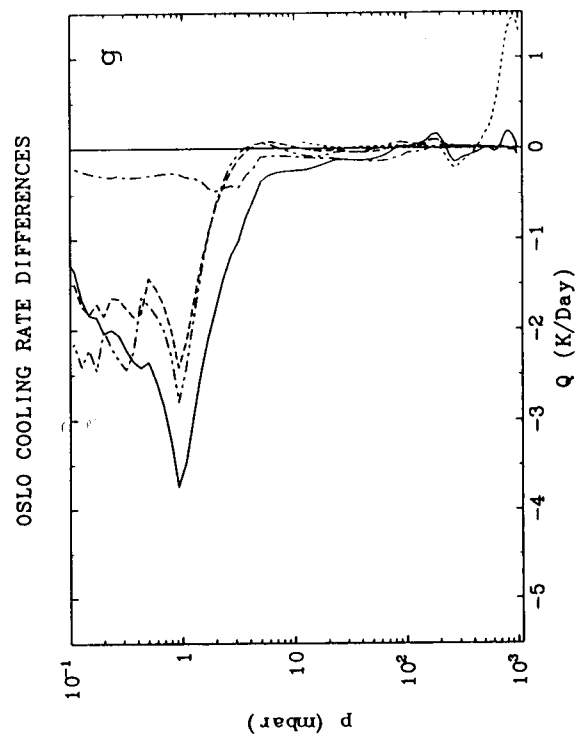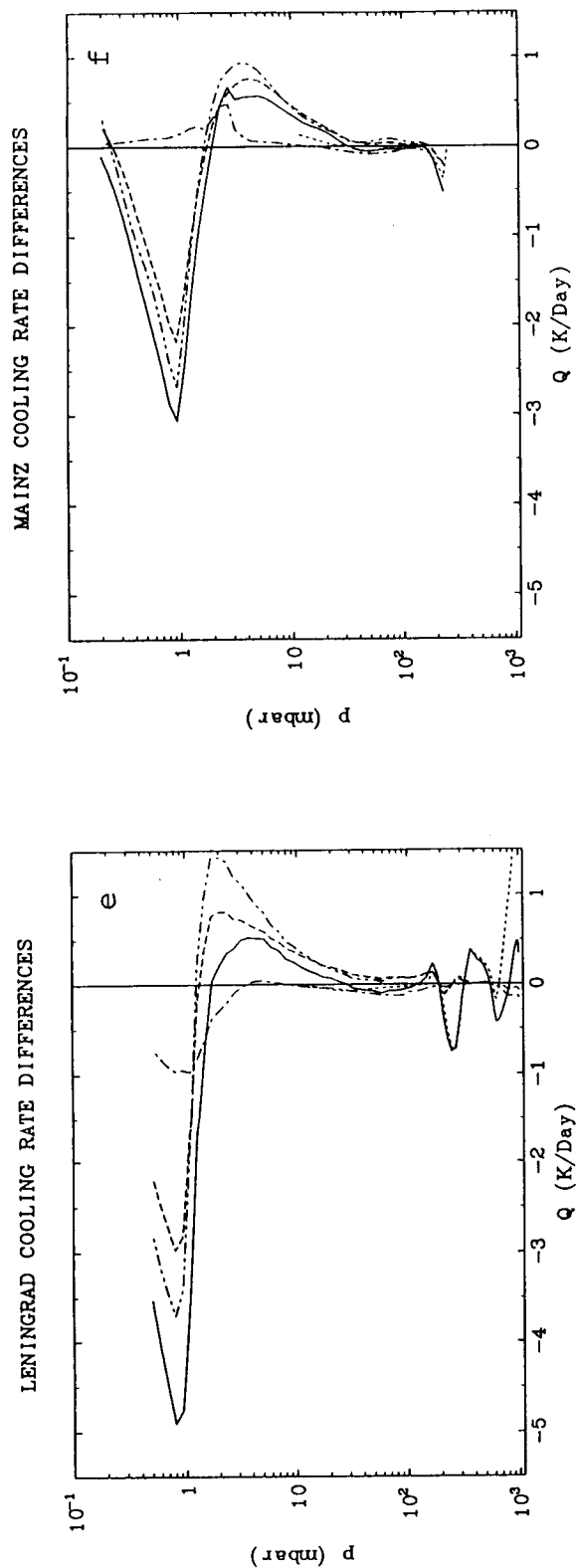
Figure 3-6 (continued). Differences between the cooling rates obtained from each model and those from the GFDL line-by-line model are shown for H_2O (dotted), CO_2 (330 ppmv, long dash; 660 ppmv, dash-dot-dot), O_3 (dash-dot), and the total cooling rate by all three gases (solid).
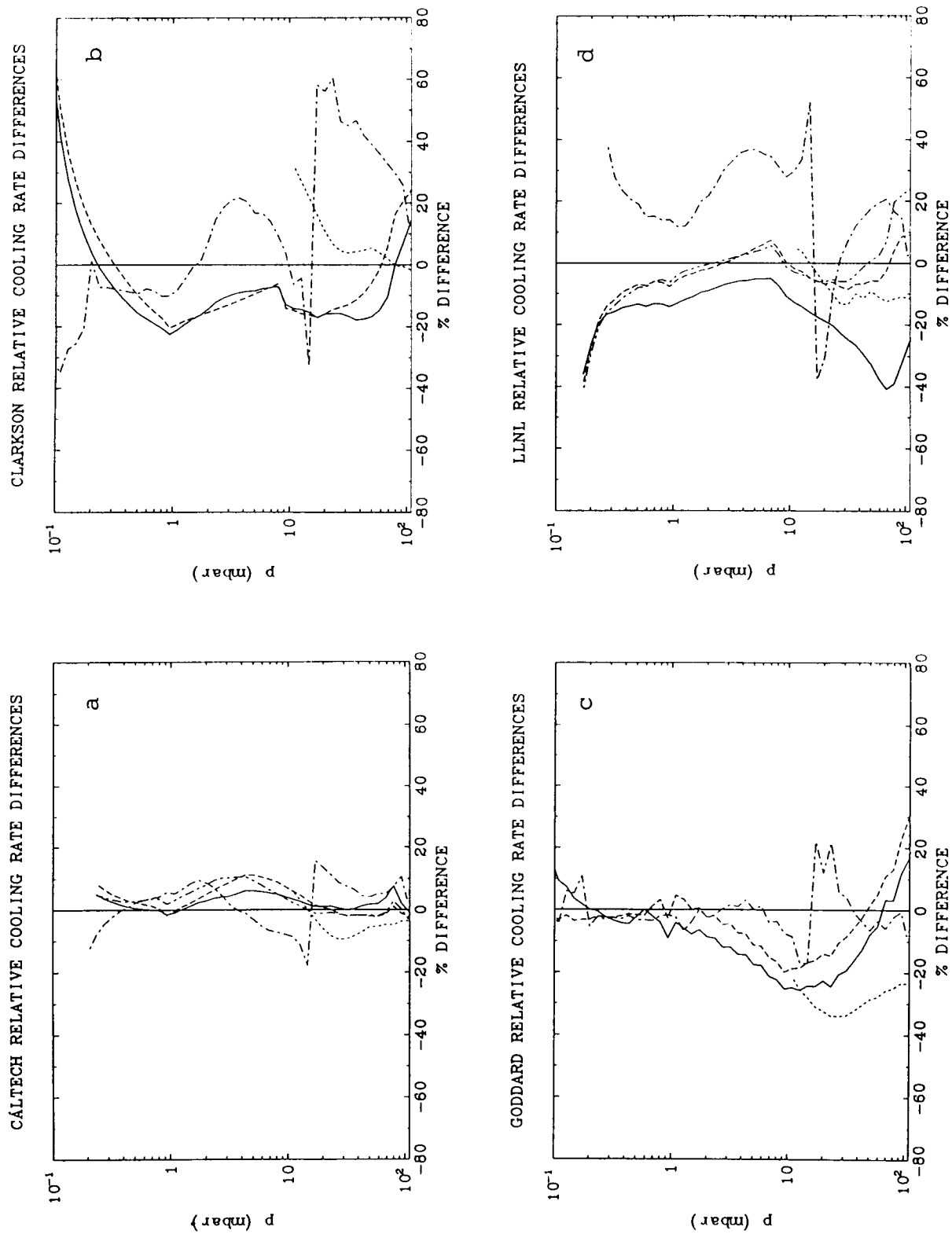
Figure 3-7. Relative differences (%) between the cooling rates obtained from each model and those from the GFDL line-by-line model are shown for H_2O (dotted), CO_2 (330 ppmv, long dash; 660 ppmv, dash-dot-dot), O_3 (dash-dot), and the total cooling rate by all three gases (solid).
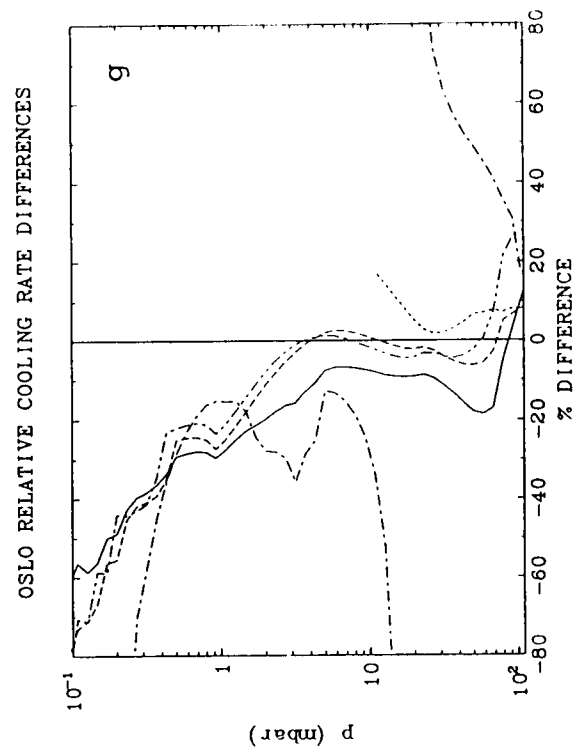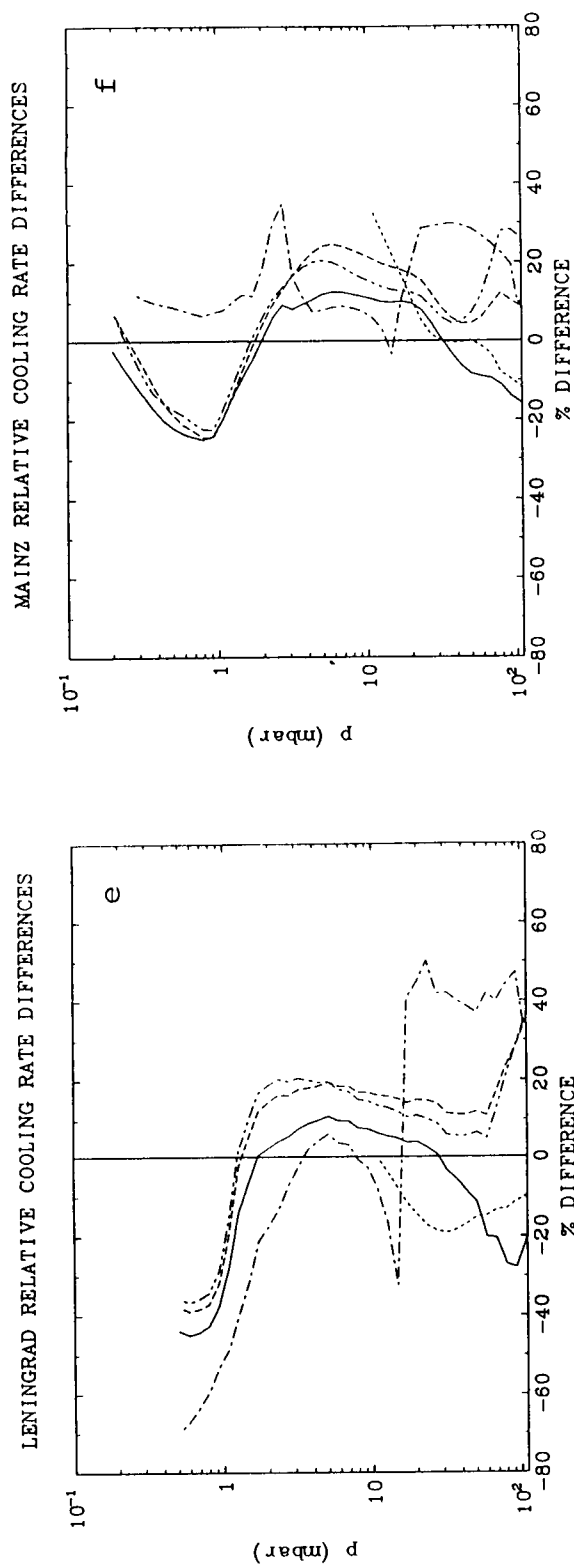
Figure 3-7 (continued). Relative differences (%) between the cooling rates obtained from each model and those from the GFDL line-by-line model are shown for H_2O (dotted), CO_2 (330 ppmv, long dash; 660 ppmv, dash-dot-dot), O_3 (dash-dot), and the total cooling rate by all three gases (solid).

```
C*********************************************************************
C*                                                                  *
C* THIS TAPE WAS GENERATED AT:                                      *
C*                                                                  *
C*             GEOPHYSICAL FLUID DYNAMICS LABORATORY / NOAA         *
C*                         PRINCETON UNIVERSITY                     *
C*                            P.O. BOX 308                          *
C*                     PRINCETON, NEW JERSEY 08542                  *
C*                           (609) 452-6500                         *
C*                                                                  *
C* QUESTIONS OR SUGGESTIONS REGARDING ITS USAGE CAN BE DIRECTED TO: *
C*                                                                  *
C*        STUART FREIDENREICH    ROOM 226    (609) 452-5279         *
C*        DAN SCHWARZKOPF        ROOM 246    (609) 452-6521         *
C*                                                                  *
C*********************************************************************
C* THIS IS A NON-LABEL, 9-TRACK, 1600 B.P.I. TAPE WRITTEN IN ASCII  *
C* FORMAT WITH A RECORD SIZE OF 80 AND BLOCK SIZE OF 4000.          *
C*********************************************************************
C*                                                                  *
C* THIS TAPE CONTAINS TWO MAIN SOURCES OF INFORMATION:              *
C*                                                                  *
C* 1.  TEMPERATURE AND MIXING RATIO (WATER VAPOR AND OZONE ONLY) DATA *
C*     AS A FUNCTION OF PRESSURE FOR VERTICAL GRIDS OF VARIOUS      *
C*     RESOLUTIONS AND ATMOSPHERIC STRUCTURES OF VARIOUS CLIMATIC   *
C*     REGIMES.                                                     *
C*                                                                  *
C* 2.  FLUX AND HEATING RATE DATA AS A FUNCTION OF FREQUENCY BAND AND *
C*     PRESSURE FOR ATMOSPHERES OF VARIOUS COMPOSITIONS, VERTICAL GRIDS*
C*     OF VARIOUS RESOLUTIONS AND ATMOSPHERIC STRUCTURES OF VARIOUS *
C*     CLIMATIC REGIMES.                                            *
C*                                                                  *
C*********************************************************************
C*                                                                  *
C* THIS TAPE IS STRUCTURED AS FOLLOWS:                              *
C*                                                                  *
C* FILE 1 CONTAINS THE TAPE DOCUMENTATION AS WELL AS A PROGRAM TO BOTH *
C* READ THE TAPE AND WRITE OUT THE DATA FOR ONE CASE.              *
C*                                                                  *
C* FILES 2 TO 20 CONTAIN THE DATA FOR THE DIFFERENT CASES. THE     *
C* CHARACTERISTICS OF EACH FILE ARE DESCRIBED BELOW:               *
C*                                                                  *
C*                          NUMBER OF      TYPE    FREQUENCY ICRCCM*
C*             ATMOSPHERIC     FLUX         OF       BAND     CASE *
C* FILE  CONSTITUENT(S)       LEVELS    ATMOSPHERE  REGION   NUMBER*
C*                                                                  *
C*   2   CO2(300PPMV)          108         MLS     0-3000CM-1   9  *
C*   3   H2O                    52         MLS     0-3000CM-1  20  *
C*   4   O3                    108         MLS     0-3000CM-1  23  *
C*   5   CO2(300PPMV)+H2O+H2O  123         MLS     0-3000CM-1  27  *
C*       CONTINUUM+O3                                               *
C*   6   CO2(300PPMV)+H2O+O3+H2O 123       MLS     0-3000CM-1   -  *
C*       CONTINUUM+CH4(1.75PPMV)+                                   *
C*       N2O(0.28PPMV)                                              *
C*   7   H2O+H2O CONTINUUM      52         MLS     0-3000CM-1  19  *
C*   8   H2O+H2O CONTINUUM      52          T      0-3000CM-1   -  *
C*   9   CO2(300PPMV)          108          T      0-2200CM-1   7  *
C*  10   CO2(600PPMV)          108         MLS     0-2200CM-1  10  *
C*  11   CO2(300PPMV)          108         MLW     0-2200CM-1  11  *
C*  12   CO2(300PPMV)          108         SAW     0-2200CM-1  15  *
C*  13   O3(1.25 X O3 IN       108         MLS     0-2200CM-1  24  *
C*       STRATOSPHERE)                                              *
C*  14   O3(0.75 X O3 IN       108         MLS     0-2200CM-1  24  *
```

104

```
C*          STRATOSPHERE)                                                   *
C*   15     CO2(300PPMV)+H2O+H2O        123           T      0-2200CM-1   25 *
C*          CONTINUUM+O3                                                     *
C*   16     CO2(600PPMV)+H2O+H2O        123          MLS     0-2200CM-1   28 *
C*          CONTINUUM+O3                                                     *
C*   17     CO2(300PPMV)+H2O+H2O        123          MLW     0-2200CM-1   29 *
C*          CONTINUUM+O3                                                     *
C*   18     CO2(300PPMV)+H2O+H2O        123          SAW     0-2200CM-1   33 *
C*          CONTINUUM+O3                                                     *
C*   19     N2O(0.28PPMV)                52          MLS     0-3000CM-1   37 *
C*   20     H2O                         108          MLS     0-2200CM-1   20 *
C*                                                                          *
C*   KEY:    MLS - MIDDLE LATITUDE SUMMER     SAW - SUBARCTIC WINTER        *
C*           MLW - MIDDLE LATITUDE WINTER     T   - TROPICAL                *
C*                                                                          *
C***************************************************************************
C*                                                                          *
C*     I N P U T    D A T A :                                               *
C*                                                                          *
C*     ICASE - EXPERIMENT CASE NUMBER (1 - 19)                             *
C*     IFILE1 - UNIT NUMBER OF INPUT FILE (30)                             *
C*     IFILE2 - UNIT NUMBER OF OUTPUT FILE (40)                            *
C*     infile - NAME OF INPUT FILE (CHARACTER*(*))                         *
C*    outfile - NAME OF OUTPUT FILE (CHARACTER*(*))                        *
C*       FMIN - MINIMUM WAVENUMBER FOR OUTPUT (CM**-1)                     *
C*       FMAX - MAXIMUM WAVENUMBER FOR OUTPUT (CM**-1)                     *
C*      ITYPE - TYPE OF OUTPUT DESIRED:                                    *
C*              1) SPECTRALLY-DEPENDENT FLUXES AND HEATING RATES.          *
C*              2) SPECTRALLY-INTEGRATED FLUXES AND HEATING RATES          *
C*                                                                          *
C* THE DATA FOR EACH FILE ARE ORGANIZED AS FOLLOWS:                        *
C*                                                                          *
C* EXPNM            : CHARACTER STRING DEFINING THE EXPERIMENT             *
C*                                                                          *
C* THE PRESSURE, TEMPERATURE AND MIXING RATIO DATA ARE WRITTEN OUT AS:     *
C*                                                                          *
C*     PFLUX, TFLUX, PDATA, TDATA, RATH2O, RATO3                           *
C*                                                                          *
C* PFLUX(I=1,NLP) : PRESSURE (IN MB) AT FLUX LEVELS                        *
C* TFLUX(I=1,NLP) : TEMPERATURE (IN K) AT FLUX LEVELS                      *
C* PDATA(I=1,NL)  : PRESSURE (IN MB) AT DATA LEVELS                        *
C* TDATA(I=1,NL)  : TEMPERATURE (IN K) AT DATA LEVELS                      *
C* RATH2O(I=1,NL) : MASS MIXING RATIO OF WATER VAPOR AT THE DATA LEVELS*
C* RATO3(I=1,NL)  : MASS MIXING RATIO OF OZONE AT THE DATA LEVELS          *
C* NL             : NUMBER OF DATA LEVELS OR NUMBER OF LAYERS              *
C* NLP            : NUMBER OF FLUX LEVELS (NL+1) (=52, 108, 123 )          *
C*                                                                          *
C* THE FLUX AND HEATING RATE DATA ARE WRITTEN OUT AS:                      *
C*                                                                          *
C*     FLX, UPFLUX, DNFLUX, HEAT                                           *
C*                                                                          *
C* FLX(I=1,NLP; N=1,NBANDS)     : NET FLUX AT FLUX LEVELS IN W/M2 FOR      *
C*                                EACH BAND                                 *
C* UPFLUX(I=1,NLP; N=1,NBANDS) : UPWARD FLUX AT FLUX LEVELS IN W/M2 FOR*
C*                                EACH BAND                                 *
C* DNFLUX(I=1,NLP; N=1,NBANDS) : DOWNWARD FLUX AT FLUX LEVELS IN W/M2      *
C*                                FOR EACH BAND                             *
C* HEAT(I=1,NL; N=1,NBANDS)     : HEATING RATE AT DATA LEVELS IN DEG/DAY*
C*                                FOR EACH BAND                             *
C*                                                                          *
C*     FLXTRP, FLXTRU, FLXTRD                                              *
C*                                                                          *
C* FLXTRP(N=1,NBANDS)           : NET FLUX AT TROPOPAUSE LEVEL IN W/M2     *
```

```
C*                                      FOR EACH BAND                         *
C* FLXTRU(N=1,NBANDS)             : UPWARD FLUX AT TROPOPAUSE LEVEL IN     *
C*                                  W/M2 FOR EACH BAND                     *
C* FLXTRD(N=1,NBANDS)             : DOWNWARD FLUX AT TROPOPAUSE LEVEL IN   *
C*                                  W/M2 FOR EACH BAND                     *
C*                                                                         *
C*      SUMFLX, SUMFLU, SUMFLD, SUMHT                                      *
C*                                                                         *
C* SUMFLX(I=1,NLP)                : SUM (OVER FREQUENCY) OF NET FLUX AT    *
C*                                  FLUX LEVELS IN W/M2                    *
C* SUMFLU(I=1,NLP)                : SUM (OVER FREQUENCY) OF UPWARD FLUX AT *
C*                                  FLUX LEVELS IN W/M2                    *
C* SUMFLD(I=1,NLP)                : SUM (OVER FREQUENCY) OF DOWNWARD FLUX  *
C*                                  AT FLUX LEVELS IN W/M2                 *
C* SUMHT(I=1,NL)                  : SUM (OVER FREQUENCY) OF HEATING RATE   *
C*                                  AT DATA LEVELS IN DEG/DAY              *
C*                                                                         *
C*      SUMTRP, SUMTRU, SUMTRD                                            *
C*                                                                         *
C* SUMTRP                         : SUM (OVER FREQUENCY) OF NET FLUX AT    *
C*                                  TROPOPAUSE LEVEL IN W/M2               *
C* SUMTRU                         : SUM (OVER FREQUENCY) OF UPWARD FLUX AT *
C*                                  TROPOPAUSE LEVEL IN W/M2               *
C* SUMTRD                         : SUM (OVER FREQUENCY) OF DOWNWARD FLUX  *
C*                                  AT TROPOPAUSE LEVEL IN W/M2            *
C* NBANDS                         : NUMBER OF FREQUENCY BANDS( = 220, 300) *
C*                                  (EACH BAND IS 10CM-1 WIDE)             *
C*                                                                         *
C*************************************************************************
C*                                                                         *
C* NOTES:                                                                  *
C*                                                                         *
C*   FLUXES WERE DETERMINED FROM LINE-BY-LINE CALCULATIONS USING THE      *
C*   AIR FORCE GEOPHYSICS LAB CATALOG OF LINES. CASES BASED ON            *
C*   FREQUENCY BANDS FROM 0-3000CM-1 USE THE 1982 VERSION, AND CASES      *
C*   BASED ON FREQUENCY BANDS FROM 0-2200CM-1 USE THE 1980 VERSION.       *
C*                                                                         *
C*   VERTICAL PROFILES OF TEMPERATURE AND MIXING RATIO OF WATER VAPOR     *
C*   AND OZONE ARE THE QUANTITIES DEPENDENT ON THE TYPE OF ATMOSPHERE     *
C*   SPECIFIED (MLS, SAW, ETC.).                                          *
C*                                                                         *
C*   TEMPERATURE PROFILES ARE FROM MCCLATCHY ET AL., 1971 AS MODIFIED     *
C*   BY THE "PTZ" PROCEDURE (FELS, 1986).                                 *
C*                                                                         *
C*   THE STANDARD CO2 VOLUME MIXING RATIOS USED ARE 300PPMV AND 600PPMV   *
C*                                                                         *
C*   THE STANDARD N2O VOLUME MIXING RATIO USED IS 0.28PPMV.               *
C*                                                                         *
C*   THE STANDARD CH4 VOLUME MIXING RATIO USED IS 1.75PPMV.               *
C*                                                                         *
C*   TROPOPAUSE LEVEL IS AS DEFINED BY THE ICRCCM PROTOCOL.               *
C*                                                                         *
C*   DATA LEVELS ARE DEFINED HALFWAY BETWEEN FLUX LEVELS.                 *
C*                                                                         *
C*   MIXING RATIO VALUES OF WATER VAPOR AND OZONE ARE WRITTEN OUT AS      *
C*   ZERO'S IF NO SUCH DATA IS USED FOR A PARTICULAR CASE.                *
C*                                                                         *
C*************************************************************************
C*                                                                         *
C* NOTES ON USAGE:                                                         *
C*                                                                         *
C*   USER DEFINES THE CASE NUMBER TO BE READ AND WRITTEN OUT AND THE      *
C*   UNIT NUMBERS FOR THE READ AND WRITE STATEMENTS IN A PARAMETER        *
```

106

```
C*    STATEMENT ( ICASE, IFILE1, IFILE2, RESPECTIVELY ).            *
C*                                                                  *
C*    USER MAY WISH TO MODIFY THE FORMAT FOR WRITING OUT THE DATA (E.G. *
C*    WRITING OUT ONLY SELECTED BANDS). NOTE HOWEVER THAT THE ARRAYS    *
C*    'FLX', 'UPFLUX', 'DNFLUX' AND 'HEAT' CAN ONLY BE READ AND WRITTEN *
C*    OUT IN THE SAME LOOP UNLESS THE ARRAYS ARE MADE TWO DIMENSIONAL   *
C*    WITH 'NBANDS' AS THE SECOND DIMENSION.                        *
C*                                                                  *
C*    THE PROGRAM CAN BE MODIFIED TO PROCESS MORE THAN ONE CASE IN A    *
C*    SINGLE RUN BY LOOPING OVER THE EXECUTABLE PORTION OF THE CODE AND *
C*    INCREMENTING THE UNIT NUMBERS IN THE READ AND WRITE STATEMENTS.   *
C*                                                                  *
C*********************************************************************
C
```